energy&fuels

pubs.acs.org/EF Article

Quantitative Characterization and Differences of the Pore Structure in Lacustrine Siliceous Shale and Argillaceous Shale: a Case Study of the Upper Triassic Yanchang Formation Shales in the Southern Ordos Basin, China

Hao Lu, Dongdong Xia, Qing Li,* Dali Yue, Shenghe Wu, Wurong Wang, and Xuemei Zhang

Cite This: *Energy Fuels* 2021, 35, 15525−15544 Read Online

ACCESS | Metrics & More | Article Recommendations

ABSTRACT: Shale oil and gas have attracted more and more attention around the world. It is particularly important to quantitatively characterize the complex pore structure of shales. Comparison of pore structure differences between different types of shales is beneficial to the exploration and development of shale oil and gas. Using the lacustrine siliceous shale (SS) and argillaceous shale (AS) of the Upper Triassic Yanchang Formation in the Ordos Basin as a case study, multiple experimental methods were introduced to quantitatively characterize full-range pore size distribution (PSD) combined with the fractal dimension theory. The experimental data of carbon dioxide adsorption, nitrogen adsorption, and high-pressure mercury injection were integrated to obtain the characterization of full-range PSD and fractal dimensions D1 to D6. The micropore surface area and volume, average mesoporous pore size, and macropore volume of SS are smaller than those of AS. On the contrary, the surface areas of mesopores and macropores, average macropore radius, and mesoporous volume of SS are slightly larger than those of AS. Commonly, the larger the pores are, the rougher the pore surfaces and the more complex the pore structures in the range of mesopores (2−50 nm) become. For macropores (pore diameter > 0.05 μm), smaller (pore diameter 0.05−1 μm) and larger (pore diameter > 17 μm) pores have rougher pore surfaces and more complex pore structures than medium pores (1−17 μm). The pore surface of SS is rougher, and the pore structure is more complex than those of AS. The interpenetrating contact relationship between quartz and clay minerals makes the pore structure more complex and reduces the porosity and permeability of AS, while the dissolution of feldspar reduces the complexity of the pore structure and improves the petrophysical properties, especially for SS. Average mesopore diameter, macropore surface area, and fractal dimension D3 and D4 can be used as reliable indexes to evaluate petrophysical properties of the shale reservoir.

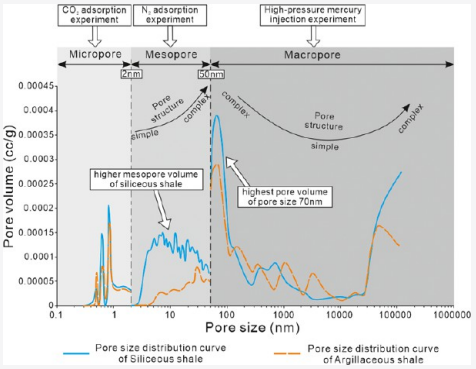

1. INTRODUCTION

Countries all over the world have a great urgent demand for fossil energy. With the development of petroleum geology, oil and gas exploration and development technology has been greatly improved.[1,2] Shale oil and gas were discovered and received a lot of attention.[3,4] The shale oil and gas in the Ordos Basin of China has great exploration and development potential.[4]

The pore system of shale is complex and various. Pore type, shape, size, distribution, and connectivity are important factors to characterize the complex microscopic pore structure, which affect reservoir quality and fluid migration.[5,6] One pore classification scheme based on the pore size was proposed by the International Union of Pure and Applied Chemistry (IUPAC),[7] which suggested that pores can be divided into three types: micropores (<2 nm), mesopores (2−50 nm), and macropores (>50 nm). The pore structure of shale can be characterized by many experimental methods. The shape, size, and location of the pores can be obtained by light microscopy (LM) and scanning electron microscopy (SEM).[8,9] It is difficult to obtain the volume data of all pores by the limited view field and two-dimensional plane of LM and SEM. The quantitative information of the pore size, pore volume, and pore surface area can be obtained by high-pressure mercury injection (HPMI), carbon-dioxide adsorption (CA), and nitrogen adsorption (NA) experiments.[6,10−13] CA and NA experiments indirectly obtain the data of micropore and

Received: June 7, 2021
Revised: September 14, 2021
Published: September 23, 2021

https://doi.org/10.1021/acs.energyfuels.1c01823
Energy Fuels 2021, 35, 15525−15544

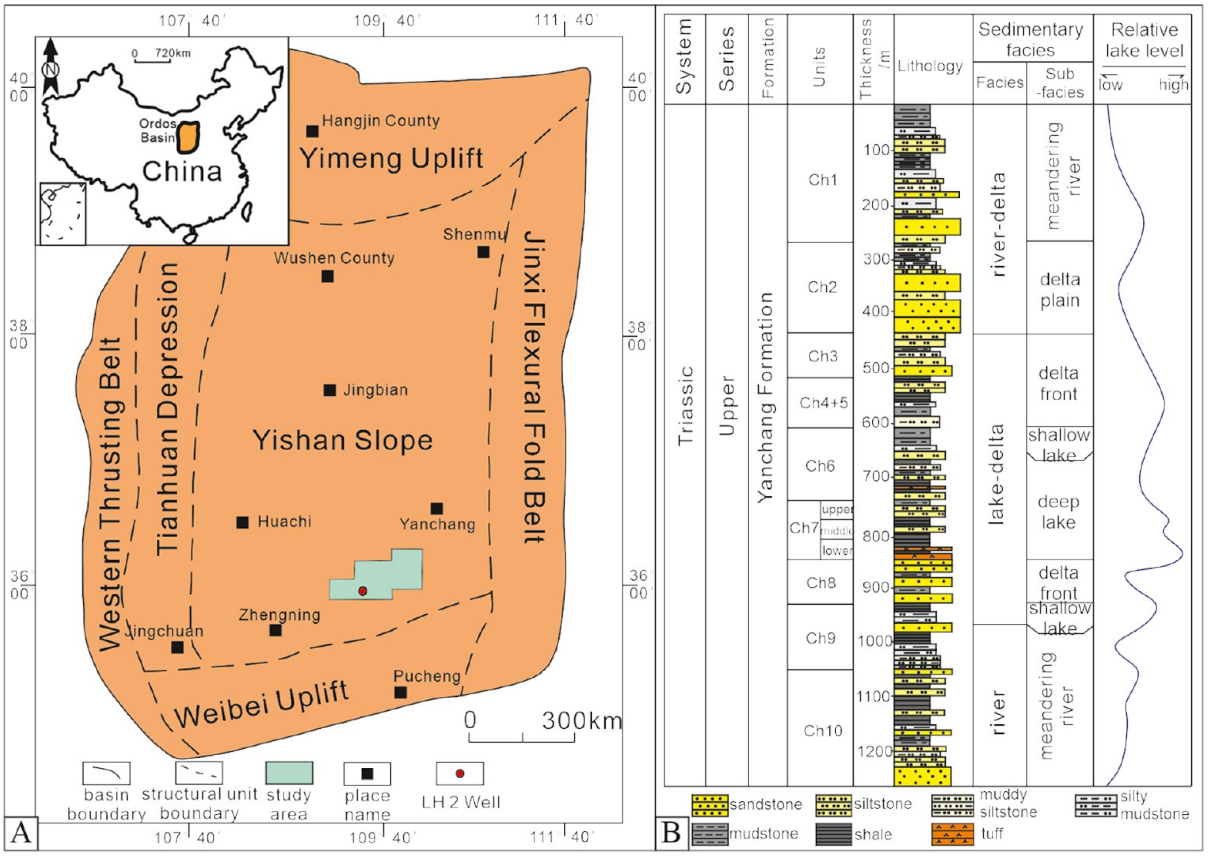

Figure 1. (A): Simplified map showing the location of the core well LH2 and the study area, the Ordos Basin of China and (B): stratigraphy, thickness, lithology, sedimentary facies and sub-facies, relative lake level in the stratigraphic chart of Yanchang Formation in the Ordos Basin.[29,30]

mesopore structure characteristics by using gas to adsorb and fill spaces of pores in rocks.[14−18] HPMI analysis is a good way to characterize the pore structure of macropores and partial mesopores.[11,19,20] Some scholars believe that the data of micropores can be obtained from CA, while mesopore and partial macropore information can be obtained by the NA experiment.[5] Due to the influence of compressibility effects, the micropore and mesopore structures cannot be accurately characterized by the HPMI experiment, while HPMI is an effective method to obtain the feature of macropore structures.[5,20] It is impossible to quantitatively characterize all pore structures, especially the full pore size distribution (PSD), by one single experimental method. In this study, three experiments have been integrated to characterize the distribution of the full-range pores.

Fractal dimension has been widely used in the characterization of the pore structure of tight sandstone and shale reservoirs. Mandelbrot first proposed the fractal concept and geometry in 1975, which is used to describe the irregularity degree and statistical self-similarity of complex objects.[21] Subsequently, many experimental methods (such as NA, HPMI, nuclear magnetic resonance, and constant-speed mercury injection) have been used to calculate the fractal dimension and quantitatively characterize the diversiform and complex structure of pores.[22−24] A higher fractal dimension commonly indicates a more complex pore structure.[25] The fractal dimension calculated by a single experimental method can only describe the characterization of the pore structure in the applicable range of the experiment, and it is difficult to obtain the fractal dimension characteristics of the full pore size. Shale has strong heterogeneity and a complex pore structure. For the Luohe area, the study area, the pore structure of shale has rarely been studied. The pore distribution characteristics of shale are not clearly understood and the influence of the pore structure on petrophysical properties is not clear. It is feasible and necessary to comprehensively characterize the shale pore structure in combination with a variety of experimental methods.

The samples in this paper were collected from the SS and AS of the Yanchang Formation in the Ordos Basin. The main aim of this study is (1) to identify the difference in characteristics of PSD between the SS and AS; (2) to calculate fractal dimensions and characterize the complex of the pore structure by CA, NA, and HPMI experiments; and (3) to find main factors influencing the pore structure and petrophysical properties of the shale reservoir.

This study is the first time to quantitatively and accurately characterize the full-range PSD characteristics of lacustrine siliceous shale (SS) and argillaceous shale (AS) in the study area and provides a profound understanding on the difference and influencing factors of the pore structure between SS and AS. This research is helpful for shale reservoir evaluation and has great significance for guiding the exploration and development of shale oil and gas.

2. GEOLOGICAL SETTING

The Ordos Basin covers parts of central and western China, with a total area of 320,000 square kilometers, ranking second among the basins in China.[26,27] The overall shape of the basin is rectangular, extending from north to south, and there are six

https://doi.org/10.1021/acs.energyfuels.1c01823
Energy Fuels 2021, 35, 15525−15544

tectonic units: Yimeng uplift at the north of the basin, Weibei uplift in the southern basin, Tianhuan depression and thrust belt in the west part of the basin, and Jinxi curved fold belt and central Yishan slope at the east and center of the basin, respectively.[26,28] The study area covers a part of the southern area of the Yishan Slope, named Luohe study area, with an area of approximately 3834 square kilometers (Figure 1A).

The differential subsidence of the basin occurred in the late period of the Indosinian movement and began to tilt from the northwest to southeast during the Late Triassic period.[31] Ordos Basin as a large multicycle craton basin is located west of the North China Platform. The basin is generally stable with a simple geological structure. There are no secondary structures inside of the basin, and faults and folds dominated by nose-like folds are developed an the edge of the basin.[32]

In the Yanchang Formation period of Late Triassic, the Ordos Basin developed complete and continuous continental lacustrine basin deposits. Some scholars divide the Yanchang Formation into five lithological sections, according to the characteristics of sedimentary cycles, electrical and lithologic assemblages, and paleontological sedimentary characteristics.[33] On the basis of lithology, oil content and vertical distribution of the oil layer, some scholars further subdivided the five lithological sections of the Yanchang Formation into ten sublayers. The formation focused on in this paper is the Chang 7 oil layer, whose thickness is about 80−120 m (Figure 1B).[34] In terms of lithology, argillaceous siltstone and siltstone are developed in the upper part layer of Chang 7, mudstone and oil shale are developed in the middle and lower parts.[33] The rock color of Chang 7 is mainly dark gray and gray-black. Among them, the gray-black shale is called "Zhangjiatan Shale", which is the key research object of this research. It is not only an important hydrocarbon source rock with good oil and gas storage capacity but also a good sign for regional stratigraphic contrast.[35]

3. SAMPLES AND METHOD

3.1. Experiment Methods. The experimental samples of shale were collected at different depths in the Chang 7 member of Yanchang Formation in Well LH2 of Luohe Oilfield (Figure 1). This study selected 48 samples for direct observation (LM and SEM), mineral quantitative analysis (X-ray diffraction), organic matter (OM) test (TOC), and porosity-related experiments (helium measuring porosity, CA, NA, and HPMI experiments).

For SEM analysis, a field-emission environmental scanning electron microscope (Quanta 200F) was used to magnify the field of view from 25 to 200 K times to observe the morphology and pore characteristics of mineral particles. The acceleration voltage is in the range of 200 V−30 kV, and the resolution can reach 1.2 nm. The instrument has three scanning modes, namely, high vacuum mode, low vacuum mode, and environmental scan mode and can also perform energy spectrum and spectrum analyses. Before the experiment, the samples need to be sprayed with carbon or gold to increase their electrical conductivity, and the observation effect will be better. The experiment was completed in the Laboratory of Energy Materials Microstructure, China University of Petroleum (Beijing).

To perform X-ray diffraction experiments, the fresh original sample of 2−3 g was ground in an agate mortar until there was no obvious particle sensation and the particle size was about 300 mesh. The ground powder was placed on the sample plate to make whole rock slice. The whole rock slice was placed in a D2 Phaser diffractometer with a 0.6 mm incident slit and an 8 mm detector slit, and a low angle attachment was placed above the sample. The scanning angle was set to 4.5−50°, step length was 0.02°, and time of each step was 0.5 or 0.6 s for measurement. Jade software was used to interpret the mineral content quantitatively.[36] The X-ray diffraction experiment was carried out in the State Key Laboratory of Petroleum Resources and Prospecting, China University of Petroleum (Beijing).

The principle of the helium porosity measurement experiment is the Boyle's law. Before testing, the system was calibrated with a standard block of known volume. The cylindrical sample (diameter 2−3 cm, length 3−5 cm) was dried at a high temperature of 105 °C and put into a CAT113 instrument to measure the porosity of the gas.

The theoretical formula of Boyle's theorem is

$$P_1 \cdot V_1 = P_2 \cdot V_2 \tag{1}$$

Particle volume calculation formula

$$V_{\text{grain}} = V_{\text{ref}} + V_{\text{matrix}} - \frac{P_1}{P_2} V_{\text{ref}} \tag{2}$$

where P_1 is the pressure in the reference chamber, MPa; V_{ref} is the volume of the reference chamber, mL; P_2 is the pressure after the helium gas diffused into the core cup, MPa; V_{matrix} is the volume of the core cup, mL; and V_{grain} is the particle volume of the sample, mL.

The total volume is calculated by measuring the diameter and length of the sample with a micrometer. The pore volume is obtained by subtracting the volume of the particles from the total volume.

$$Ø = \frac{V_p}{V_b} \times 100\% \tag{3}$$

where V_p is the pore volume, cm^3 and V_b is the total volume, cm^3.

The permeability measurement method was complied with the standard core routine analysis method SY/T5336-2006 of the Oil and gas industry of the People's Republic of China. All cylindrical samples (diameter 2−3 cm, length 3−5 cm) were dried to constant weight at 105 °C before testing, and the system was calibrated with a standard block with known permeability before testing. A high and low permeability meter CAT112 was used. The sample was sealed in a hassler gripper with a 200psi ring pressure, dry air was allowed to pass steadily through the sample to measure the inlet and outlet pressures and the flow rate of the air.

The calculation formula of Darcy's law for gas seepage is

$$K = 2000 \frac{P_{\text{atm}} \mu Q_a L}{A(P_1^2 - P_2^2)} \tag{4}$$

where K is the permeability, 10^{-3} μm^2; P_{atm} is the total volume, atm; μ is the gas viscosity, mPa·s; P_1 is the inlet pressure, atm; P_2 is the outlet pressure, atm; Q_a is the flow velocity, mL; A is the sectional area, cm^2; and L is the length, cm.

The pore parameters of micropores and mesopores were obtained from CA and NA experiments.[5,37] The isothermal adsorption experiments of carbon dioxide and nitrogen were performed using an automatic specific surface and PSD analyzer Autosorb-iQ and Quadrasorb Station 3−6.0. The crushed shale samples (60−80 mesh) were dried in an oven at

https://doi.org/10.1021/acs.energyfuels.1c01823
Energy Fuels 2021, 35, 15525−15544

110 °C for 12 h and then degassed for 12 h in an analyzer under a vacuum condition of 110 °C. The CA experiment was experimentally adsorbed with carbon dioxide at 0 °C (273.15 K). In the NA experiment, nitrogen was used as an adsorbent at −196 °C (77 K), and the adsorption amount of gas under different relative pressures was measured. After the test, the CA data and NA data were interpreted by the density functional theory model to obtain pore volume, specific surface area, and PSD. The specific surface area of macropores is obtained by subtracting the specific surface area of micropores and mesopores from the total specific surface area of NA data.

The HPMI method is based on the capillary bundle model and assumes that the porous media consists of capillary bundles with unequal diameters. The American CoreLab CMS300 and AutoPore IV 9505 mercury intrusion instruments were used during the HPMI test. The cylindrical samples (diameter 2−3 cm, length 3−5 cm) that have been dried at a high temperature of 105 °C were subjected to mercury injection and mercury removal experiments at a maximum test pressure of 200 MPa to obtain the pore radius, sorting coefficient, displacement pressure, and other related parameters.[38,39] The calculation formula of the pore distribution curve and capillary pressure curve is

$$P_c = \frac{2\sigma \cos\theta}{r} \tag{5}$$

where P_c is the capillary pressure, MPa; σ is the interfacial tension between mercury and air, the value is 480 dyn/cm; θ is the wetting angle between mercury and rock, the value is 140°; and r is the pore radius, μm.

The maximum pore radius r_{max} (μm) is

$$r_{max} = \frac{0.7354}{P_d} \tag{6}$$

where P_d is the displacement pressure, MPa.

The median pore radius r_{50} (μm) is

$$r_{50} = \frac{0.7354}{P_{50}} \tag{7}$$

where P_{50} is the saturation median pressure, MPa.

The average pore radius $\overline{r}$ (μm) is

$$\overline{r} = \frac{\sum (r_{i-1} - r_i)(S_i - S_{i-1})}{2\sum (S_i - S_{i-1})} \tag{8}$$

where r_i is the pore radius at a point, μm and S_i is the mercury saturation at a point, %.

According to the Chinese national standard GB/T19145-2003 "Determination of Total Organic carbon in Sedimentary Rocks", a LECO CS230 carbon and sulfur analyzer from the United States was used to test TOC. The principle of total organic carbon detection is to remove the inorganic carbon in the sample with dilute hydrochloric acid and then burn it in the high-temperature oxygen flow, so that the total organic carbon is converted into carbon dioxide, and the content of total organic carbon is detected by an infrared detector. The ambient temperature is 25 °C and the relative humidity is 28%. In the detection conditions, the carrier gas pressure was set as 0.27 MPa and the oxygen purity was 99.5%. The flow rate of combustion gas was 2 L/min and that of analysis gas was 0.5 L/min.

3.2. Calculation of Fractal Dimensions. The roughness of pore surface and complexity of the pore structure can be indicated by the fractal dimension.[40−42] The fractal dimension is generally within the range of 2.0−3.0.[13,43] A completely irregular or rough pore surface corresponds to a maximum value of 3 and a smooth hole surface corresponds to a value of 2. There is a positive correlation between the fractal dimension and the heterogeneity of the pore structure.[11]

3.2.1. Fractal Dimensions of Micropores Calculated by CA Experiment. Jaroniec assumed that the minimum of the pore size x_{min} is 0.1 nm and the maximum of the pore size x_{max} is 1.0 nm and found that there was an obvious linear relationship of the log−log curve of the pore size x and the distribution function $J(x)$ of the pore size and at the micropore scale.[44]

$$\ln J(x) = (2 - D_m)\ln x + C \tag{9}$$

where D_m is the fractal dimension of the micropore.

$$J(x) = \frac{3\rho^{\nu}}{\Gamma\left(\frac{\nu}{3}\right)} \cdot \frac{z^{\nu-1} \cdot e^{-(\rho z)^3}}{15 + 8557.5z^2 - 0.014z^{-2}} \tag{10}$$

where ρ is the scale parameter, kJ/mol and ν is the shape parameter, dimensionless. $\rho > 0$, $\nu > 0$, $\Gamma(x)$ is Gamma function.

Dubinin and Stoeckli believed that the adsorption process of micropores is the filling of their internal volume, rather than the layered adsorption on the pore wall. Pore filling degree θ was used to indicate the capacity of adsorption[45]

$$\theta = \frac{V}{V_0} \tag{11}$$

where V represents the volume of pores filled under the equilibrium pressure of P, cm^3/g and V_0 represents the total volume of micropores, cm^3/g.

Dubinin-Radushkevich (D-R) equation

$$\ln V = \ln V_0 - s \ln^2\left(\frac{P_0}{P}\right) \tag{12}$$

$$s = \frac{2.303}{k}\left(\frac{RT}{\beta}\right)^2 \tag{13}$$

where R represents the gas constant, the value is 8.314 J/(mol·K); T represents the Kelvin temperature, K; P and P_0 are, respectively, adsorption pressure and saturated vapor pressure, MPa.

Because z is a function of characteristic energy, and the characteristic energy is related to the micropore size x, Stoeckli found the following relationship between x and z[46]

$$x = 15 + 8557.5z^2 - 0.014z^{-2} - 0.75 \tag{14}$$

The parameters ρ, ν, and z were substituted into eq 2 to obtain $J(x)$. According to eq 1, the fractal dimension D_m of micropores was obtained by the slope of the linear relation between $\ln J(x)$ and $\ln x$.

3.2.2. Fractal Dimensions of Mesopores Calculated by NA Experiment. The mesoporous fractal dimension was calculated by using the isothermal data of adsorption branches obtained from NA experiments and the FHH model.[47,48] The appropriate formula for calculating the fractal dimension should ensure that the fractal dimension is within the square of the reasonable interval and the data fitting degree is good. The following calculation formula is selected[49,50]

https://doi.org/10.1021/acs.energyfuels.1c01823
Energy Fuels 2021, 35, 15525−15544

$$\ln V = a \cdot \ln\left[\ln\left(\frac{P_0}{P}\right)\right] + C \tag{15}$$

$$D = a + 3 \tag{16}$$

where V (cc/g) represents the volume of the adsorbed gas at the equilibrium pressure P (MPa), a represents the slope value of the fitting line between ln V and $\ln[\ln(P_0/P)]$, P_0 represents the pressure of saturated vapor, MPa, and C is a constant. D is the fractal dimension.

3.2.3. Fractal Dimensions of Macropores Calculated by HPMI Experiment. The Li model is widely used to calculate the fractal dimension using experimental data from the high-pressure mercury intrusion experiment.[13,51] The data from the actual experiment are in good agreement with fractal dimensions calculated by this model. This article uses the following calculation formula

$$\lg(S_{Hg}) = K \cdot \lg(P_C) + C \tag{17}$$

$$D = K + 2 \tag{18}$$

where S_{Hg} represents mercury saturation in %, K represents the slope of the straight line between $\lg(S_{Hg})$ and $\lg(P_C)$, P_C represents the capillary pressure, MPa, and C represents a constant. D is the fractal dimension.

4. RESULTS

The lacustrine shale "Zhangjiatan Shale" of the Chang 7 Member in the Ordos Basin is taken as the research object in this study. On the basis of the relative content of siliceous minerals and argillaceous minerals, SS and AS were distinguished. According to pore morphology and genetic mechanism, various types of pores have been identified in the lacustrine shales, such as inorganic pores (i.e., interparticle and intraparticle pores, intercrystalline pores, and interlamellar pores), OM pores, and microfractures. Pore and permeability data of the lacustrine shales were obtained by the helium gas experiment.

4.1. Mineral Compositions, Pore Types, and Petrophysical Properties. The surface color of lacustrine SS is grayish-black. The sandy laminae and the organic-rich laminae are alternately developed in lacustrine SS (Figure 2A,B). The mineral types are mainly siliceous minerals, including quartz, feldspar, and a small percentage of pyrite and carbonate minerals (Figure 3A). The quartz content of lacustrine SS ranges from 14.9 to 22.12 wt %, with an average of 19.03 wt %, and the feldspar content varies between 35.7 and 46.7 wt % (average 40.49 wt %). The content of clay minerals varies from 25.38 to 40.8 wt %, with an average of 34.43 wt % (Figure 3A,B). The content proportion of carbonate minerals ranges between 4.8 and 10.81 wt % (average 7.81 wt %). The TOC of lacustrine SS ranges from 2.99 to 3.95% (average 3.47%). The pore types are mainly interparticle pores, OM pores, and intercrystalline pores, with a few interlamellar pores and microfractures (Figure 4).

The lacustrine AS has black color, with alternating light and dark laminae (Figure 2C,D). The dark laminae are mainly mixed laminae of clay and OM (Figure 2E), while the light laminae are composed of crystal pyroclasts or silt sand (Figure 2F). The mineral types are dominated by clay minerals, followed by siliceous minerals such as quartz and feldspar, with a small proportion of pyrite and carbonate minerals (Figure 3A). The content of clay minerals accounts for nearly half of the total mineral content, ranging between 47.1 and 59.5 wt % (average 54.23 wt %) (Figure 3A,B). The quartz content of lacustrine AS varies from 10.3 to 13.1 wt %, the average of 11.45 wt %, and the feldspar content varies between 24.8 and 33.1 wt % (average 27.8 wt %). In addition, the content of carbonate minerals ranges between 4.8 and 10.81 wt %, with an average of 7.81 wt %. The pyrite content of sample no. 6 is only 1.7 wt %. The TOC varies between 1.85 and 7.42%, with an average of 4.8%. The pore types of AS are mainly interlamellar pores, interparticle pores, and OM pores, which are different from those of SS. The proportion of intercrystalline pores and microfractures is low (Figure 4).

The petrophysical properties of SS are poor, with low porosity (1.52−2.94%, average 2.22%) and permeability (0.00025−0.00044 mD, average 0.00035 mD). An anomalous point is from sample no. 8 (2.37%, 0.187 mD), and the abnormally high permeability is due to the development of fractures in the sample. The petrophysical properties of AS are similar as those of SS. The porosities of lacustrine AS range from 1.81 to 2.67%, with an average of 2.2%. The permeabilities vary between 0.00025 and 0.00044 mD (average 0.00038 mD). Except for the special point (2.37%, 0.187 mD), the porosity of lacustrine SS and AS is positively correlated

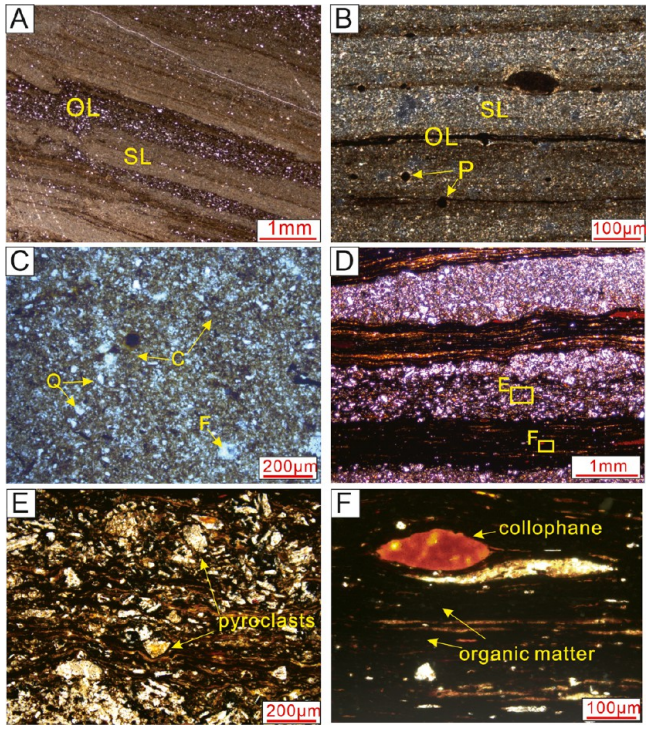

Figure 2. (A) Microscopy image of SS displaying that "OL" represents the organic-rich laminae, "SL" represents the sandy laminae, the sample from the Well LH2, 929.82 m. (B) Image of SS by a microscope displaying that "OL" represents the organic-rich laminae, "SL" represents the sandy laminae, "P" represents the pyrite, the sample from the Well LH2, 970.99 m. (C) Microscopy image of AS under single polarized light, "Q" represents the quartz, "F" represents the feldspar, "C" represents the minerals of clay, the sample from the Well LH2, 935.02 m. (D) Microscopy image of AS under single polarized light shows alternating light and dark laminae from the Well JH4, 1452.5 m. "E" is the light laminae, "F" is the dark laminae. (E) Microscopy image of the light laminae composed of crystal pyroclasts or silt sand in AS under single polarized light. (F) Microscopy image of the dark laminae developed with the collophane AS under single polarized light.

https://doi.org/10.1021/acs.energyfuels.1c01823
Energy Fuels 2021, 35, 15525−15544

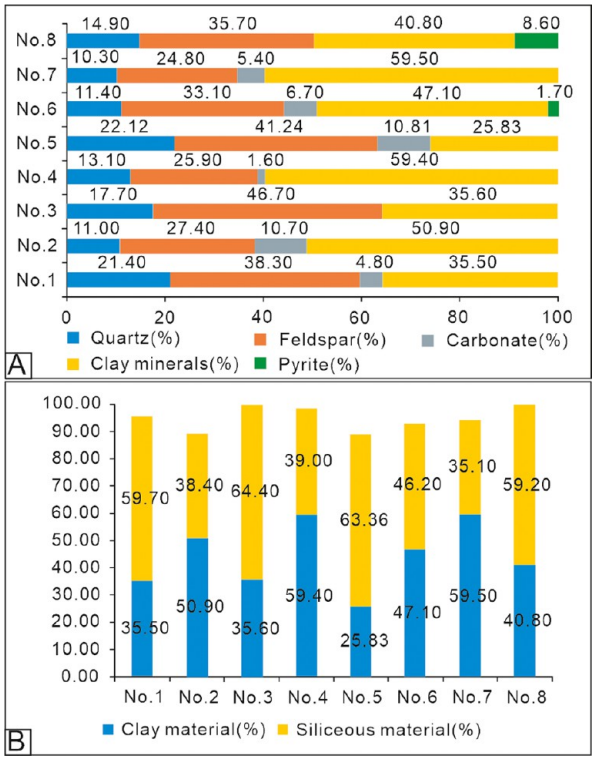

Figure 3. (A) Histogram of average minerals content of shales in Well LH2. (B) Relative content of siliceous minerals and argillaceous minerals content of shales in Well LH2.

with permeability, with the correlation coefficient (R^2) of 0.7958 (Figure 5).

4.2. Pore Structure Characterized by CA, NA, and HPMI. *4.2.1. Microporous Structure Characterized by CA.* There are some differences in the micropore structure between SS and AS. In the relative pressure (P/P_0) range of 0−0.03, the adsorption capacity of carbon dioxide of AS is higher than that of SS, reaching 0.429−0.8767 cc/g, and the adsorption capacity of carbon dioxide of SS varies from 0.2658 to 0.6927 cc/g (Figure 6A). The difference of the average micropore size between SS and AS is very small. The average micropore size of SS ranges between 1.19 and 1.25 nm and that of AS varies from 1.19 to 1.23 nm. It indicates that the micropores of SS and AS are mainly OM pores, and the difference of the pore size of OM pores is small. The micropore surface area and volume of AS are slightly higher than that of SS. The micropore surface of AS ranges between 7.82 and 9.76 m^2/g, while the micropore surface area of SS is 5.48−7.55 m^2/g. The micropore volume of AS varies between 0.0018 and 0.004 cc/g, while the micropore volume of SS is 0.0012−0.003 cc/g (Table 1).

4.2.2. Mesoporous Structure Characterized by NA. International Union of Pure and Applied Chemistry (IUPAC) divided the isotherm adsorption curves into six types (type I−VI),[52] with four types of the hysteresis loops (H1−H4). The isothermal adsorption curves of SS and AS are mainly of type IV, indicating that both shales are dominated by mesopore capillary condensation. There is no saturation when the pressure is close to the maximum, indicating that the pore system of shale is continuous with complete range of nanometer to micron.[23]

The hysteresis loops of sample no. 3 in SS and AS are mainly type H3 (Figure 6B), indicating the development of trough

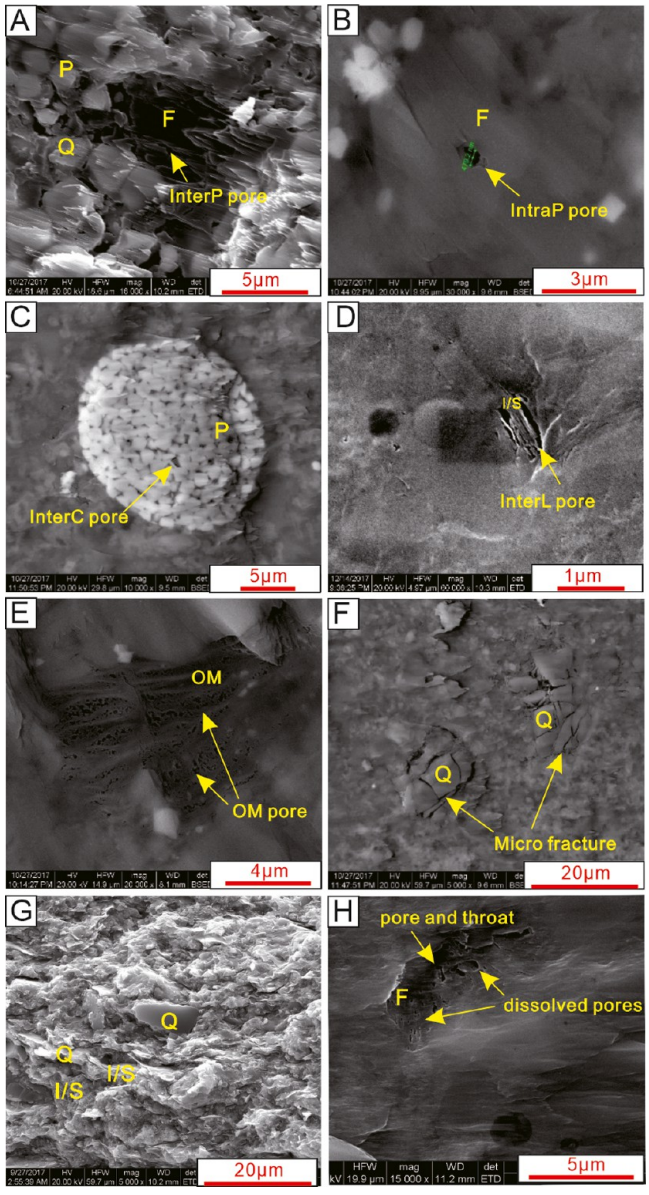

Figure 4. Examples of different pore types in the lacustrine shales obtained from the Yanchang Formation. (A) Interparticle (InterP) pores occur at the edge of quartz minerals and feldspar minerals, "Q" represents the quartz, "F" represents the feldspar, "P" represents the pyrite, from Well LH2, 970.99 m. Observed by SEM. (B) Intraparticle (IntraP) pores within the feldspar from Well LH2, 970.99 m. Observed by SEM. (C) Intercrystalline (IntraC) pores within the pyrite framboid from Well LH2, 966.26 m. Observed by SEM. (D) Interlamellar (IntraL) pores within illite/smectite from Well LH2, 929.82 m. Observed by SEM. (E) Micropores within OM from Well LH2, 970.99 m. Observed by SEM. (F) Microfractures within quartz grains from Well LH2, 966.26 m. Observed by SEM. (G) Quartz and clay minerals show interpenetrating contact relations with each other, "I/S" is illite/smectite formation, from Well LH2, 966.26 m, observed by SEM. (H) Dissolved pores and throats developed in the feldspar mineral, from Well LH2, 966.26 m, observed by SEM.

pores or disordered lamellar pores and narrow wedge-shaped pores. The hysteresis loops of samples no. 1 and no. 5 in SS are between H2 and H3 types (Figure 6B), indicating that SS develop not only fluted pores or disordered lamellar pores and narrow wedge-like pores formed by the stacking of lamellar particles but also fine diameter and ink-bottle pores or

https://doi.org/10.1021/acs.energyfuels.1c01823
Energy Fuels 2021, 35, 15525−15544

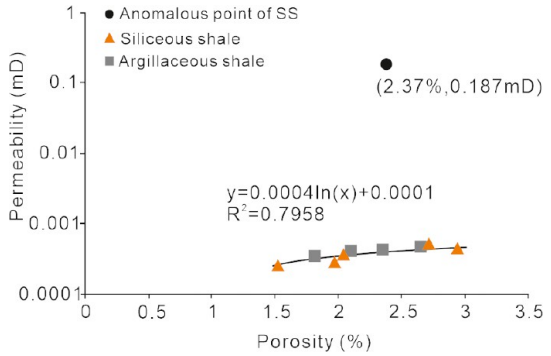

Figure 5. Cross-plot was drawn by data of porosity and permeability in lacustrine shales obtained from Yanchang Formation. An anomalous point is from sample no. 8 (2.37%, 0.187 mD) of SSs.

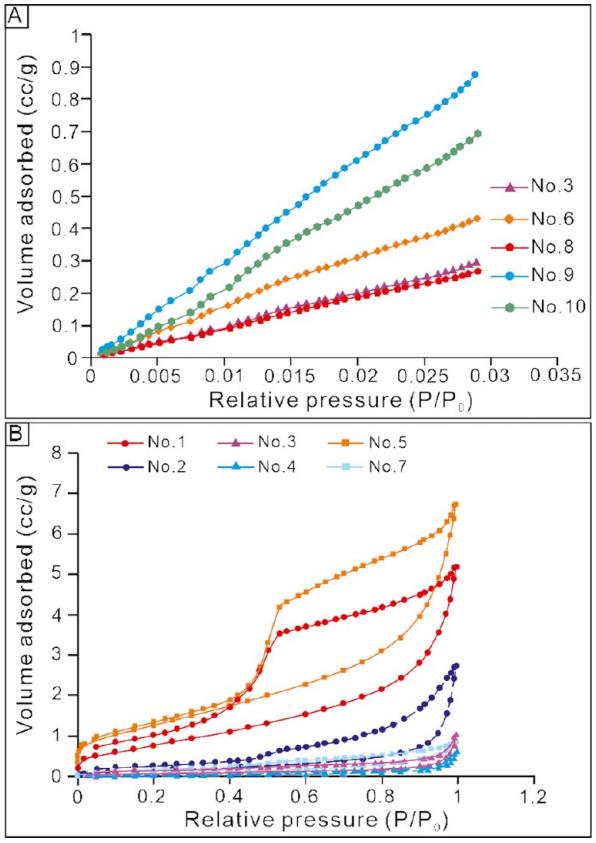

Figure 6. (A) Isothermal adsorption curves obtained from CA experiments of shale samples (no. 3, no. 6, no. 8, no. 9, and no. 10) from Yanchang Formation shales. no. 3, no. 8, and no. 10 are the samples of SSs, no. 6 and no. 9 are the samples of ASs. (B) Isothermal adsorption and desorption curves obtained from the NA experiments of six representative samples (no. 1, no. 2, no. 3, no. 4, no. 5, and no. 7) from the Yanchang Formation shales. no. 1, no. 3, and no. 5 are the samples of SSs, no. 2, no. 4, and no. 7 are the samples of ASs.

columnar and spherical pores. In particular, the content of siliceous minerals in sample no. 3 is higher than that of clay minerals, but the absolute clay minerals content is high, so the pore structure characteristic of sample no. 3 is similar to that of AS. The above characteristics indicate that the mesoporous pore structure of shales is complex and there are differences in the mesoporous pore structure between different kinds of shales, as well as among the same kind of shales.

Table 1. Average Micropore Diameter, Micropore Surface Area, and Total Micropore Volume Obtained from CO_2 Adsorption Isotherms[a]

samples	lithologies	depth (m)	AMiD (nm)	MiSA (m^2/g)	TMiV (cc/g)
no. 3	SS	929.82	1.23	5.4810	0.0013
no. 6	AS	966.26	1.19	7.8240	0.0018
no. 8	SS	970.99	1.25	5.5500	0.0012
no. 9	AS	1452.5	1.23	9.7620	0.0040
no. 10	SS	1453.62	1.19	7.5480	0.0030

[a]SS = siliceous shale; AS = argillaceous shale; AMiD = average micropore diameter; MiSA = micropore surface area; and TMiV = total micropore volume.

The surface area of the mesopore of SS ranges from 0.2119 to 3.8179 m^2/g (average 2.1807 m^2/g), while the surface area of the mesopore of AS is relatively small, mainly between 0.12 and 0.6011 m^2/g, with an average value of 0.3456 m^2/g. The surface areas of the macropores in SS and AS are 0.0153–0.0411 and 0.0072–0.0414 m^2/g, respectively. Obtained from the NA experiments, the total mesoporous volumes of SS and AS are 0.0031–0.0092 and 0.0009–0.0026 cc/g, respectively, indicating that the surface area of macropores and total mesoporous volumes in AS are both slightly smaller than those in SS. The average mesoporous pore size of SS is smaller than that of AS, with averages of 14.34 and 22.14 nm, respectively (Table 2).

Table 2. Mesopore and Macropore Surface Area, Mesopore Volume, and Average Mesopore Diameter Obtained from N_2 Adsorption–Desorption Isotherms[a]

samples	lithologies	depth (m)	MeSA (m^2/g)	MaSA (m^2/g)	TMeV (cc/g)	AMeD (nm)
no. 1	SS	877.36	2.5124	0.0411	0.0064	10.21
no. 3	SS	929.82	0.2119	0.0153	0.0031	23.96
no. 5	SS	939.46	3.8179	0.0399	0.0092	8.84
no. 2	AS	927.97	0.6011	0.0414	0.0026	23.63
no. 4	AS	935.02	0.1200	0.0084	0.0009	26.86
no. 6	AS	966.26	1.6397	0.1278	0.0059	14.04
no. 7	AS	970.29	0.3156	0.0072	0.0013	15.92

[a]SS = siliceous shale; AS = argillaceous shale; MeSA = mesopore surface area; MaSA = macropore surface area; TMeV = total mesopore volume; AMeD = average mesopore diameter.

4.2.3. Macroporous Structure Characterized by HPMI. The capillary pressure curves of SS and AS are similar (Figure 7), slightly upward to the right, and the mercury entry section in the middle is relatively gentle. When the capillary pressure is about 10 MPa, a large amount of mercury starts to be injected into the shale, and the displacement pressure is both high, indicating that the pore sizes of SS and AS are generally small and mercury can only be injected into the connected pores of the shales under a higher capillary pressure.

The maximum mercury saturation of SS and AS is close, with averages of 77.17 and 79.92%, respectively. However, the maximum mercury saturation of sample no. 5 in SS is low, which makes the mercury saturation of SS slightly lower than that of AS. This is because the sample has a higher clay mineral content compared with other SS and more complex pore structure makes it more difficult for mercury to be injected into pores. The efficiency of mercury withdrawal of SS ranges from 71.38 to 89.11%, with an average of 82.87%. The efficiency of

https://doi.org/10.1021/acs.energyfuels.1c01823
Energy Fuels 2021, 35, 15525–15544

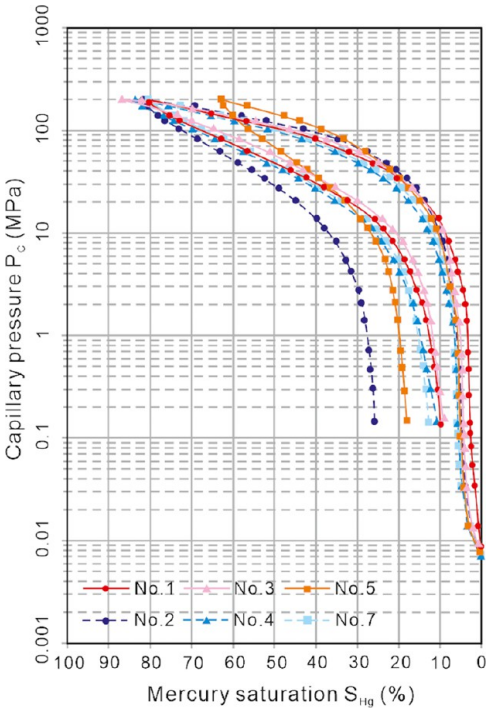

Figure 7. Capillary pressure curves obtained from HPMI of six representative samples from Yanchang Formation shales. no. 1, no. 3, and no. 5 are the samples of SSs, no. 2, no. 4, and no. 7 are the samples of ASs.

mercury withdrawal of AS varies between 68.46 and 86.97%, with an average of 79.92%. The efficiency of mercury withdrawal of samples no. 2 and no. 5 is slightly lower than those of the other samples, also indicating that the pore structure is more complex (Table 3).

The maximum macropore radius of SS and AS is similar, with an average value of 53.36 and 53.37 nm, respectively. The average macropore radius of SS is slightly higher than that of AS, with an average of 12.09 and 11.5 nm, respectively. The median macropore radius of SS is slightly lower than that of AS (average of 6.44 and 7.18 nm, respectively) (Table 3).

The sorting coefficient of pore sizes in SS is similar to that of AS, with average values of 1.25 and 1.28, respectively, indicating that the macropore distribution characteristics of SS and AS are similar. The distribution diagrams of the pore size show that the frequency of the macropore diameter distribution is high at both ends, low at the middle size, and the lowest value of frequency appears approximately at a pore size of 160 nm (Figure 8). With the effective pore size increasing, the contribution of the pore size to permeability is increases. The contribution of the macropore size around 400 nm to permeability is the largest.

4.3. Reservoir Fractal Characteristics. *4.3.1. Fractal Dimensions of Micropores.* Based on the data obtained from the CA experiment, the fractal dimensions denoted as D1 of micropores in SS and AS were calculated, which were both within the range of 2−3 (Table 4). The linear fitting degree R^2 of the logarithm of pore size function A and pore size B is above 0.9 (Figure 9A−C), indicating that D1 can effectively indicate the structure complexity and the surface roughness of micropores.

The fractal dimension D1 of SS is larger than that of AS, showing that the micropore structure of SS is more complex than that of AS. As shown in Table 4, the TOC of SS is low. In addition to some organic pores, there are also micropores related to inorganic minerals in the micropores. The diversity of micropore types makes the micropore structure more complex. AS has a higher TOC and a greater proportion of organic pores in micropores, which reduces the diversity of micropores and makes the pore structure relatively simple.

4.3.2. Fractal Dimensions of Mesopores. The fractal dimensions of SS are divided into two sections in the relative pressure (P/P_0) range of 0.01−0.9 and 0.9−1, which are D2 and D3, respectively (Figure 9D−H). The fractal dimension D2 ranges from 2.40 to 2.54, with an average of 2.46. The fractal dimension of D3 varies from 2.47 to 2.83, and the average value is 2.69 (Table 5).

Different from SS, the fractal dimensions of AS are divided into two sections by relative pressures (P/P_0) of 0.02−0.9 and 0.9−1. The fractal dimension of D2 and D3 can be utilized to describe the pore structure characteristics. The fractal dimension D2 ranges from 2.33 to 2.44 (average 2.39), and the fractal dimension D3 varies between 2.52 and 2.76 (average 2.60).

The fractal dimension D2 is less than D3 of the same type of shales, indicating that larger pores have rougher pore surfaces and more complex pore structures. For different types of shales, the fractal dimensions of SS are larger than those of AS, indicating that the pore surface of SS is rougher, with more complex pore structures. Taking sample no. 5 of SS as an example, clay and silica contents are 25.83 and 63.36%, respectively, and the ratio between the content of clay mineral and siliceous mineral is the minimum. There are quartz interparticle pores, interparticle pores and intraparticle pores of feldspar minerals, interparticle pores of clay minerals and OM pores. Due to various mineral types and the influence of

Table 3. Some Parameters of the Macropore Structure of the Yanchang Formation Shales Obtained from the HPMI Experiment[a]

				pore radius (nm)					
samples	lithologies	Φ (%)	K (mD)	Max	Ave	Med	Sc	Mms (%)	Emw (%)
no. 1	SS	1.52	0.00025	53.35	12.26	7.18	1.25	81.85	88.12
no. 3	SS	2.94	0.00044	53.36	11.56	6.72	1.22	86.86	89.11
no. 5	SS	2.04	0.00037	53.36	12.45	5.43	1.27	62.81	71.38
no. 2	AS	2.25	0.00029	53.36	10.63	6.23	1.21	81.97	68.46
no. 4	AS	1.81	0.00035	53.36	11.96	7.88	1.33	83.72	86.97
no. 7	AS	2.65	0.00047	53.36	11.91	7.42	1.30	80.51	84.32

[a]SS = siliceous shale; AS = argillaceous shale; Φ = porosity; K = permeability; Max = maximum; Ave = average; Med = median; Sc = sorting coefficient; Mms = maximum mercury saturation; Emw = efficiency of mercury withdrawal.

https://doi.org/10.1021/acs.energyfuels.1c01823
Energy Fuels 2021, 35, 15525−15544

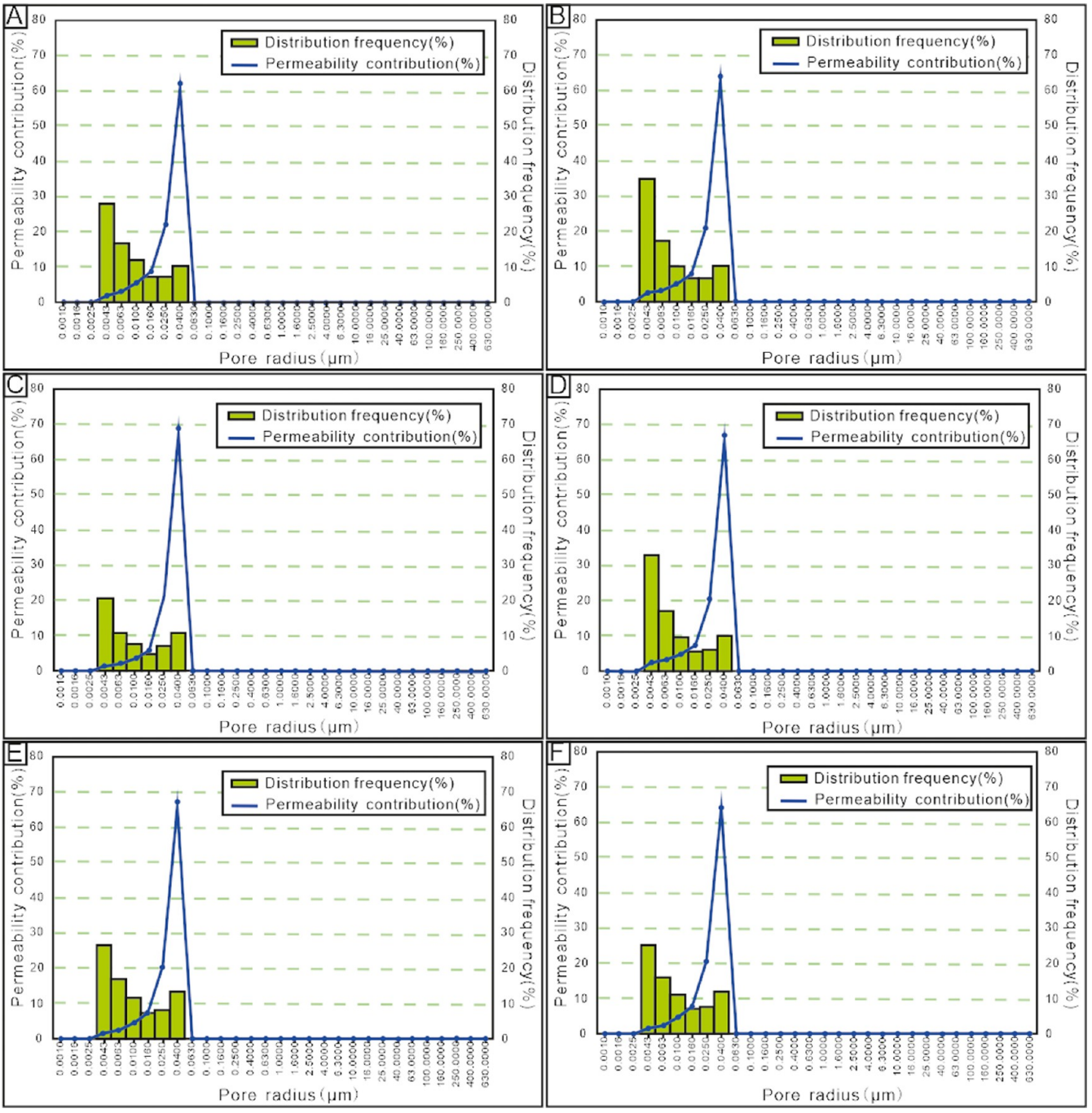

Figure 8. Histogram of pores radius distribution frequency and the curve graph of permeability contribution of six representative samples from the Yanchang Formation shales. (A) Sample no. 1 of SSs. (B) Sample no. 3 of SSs. (C) Sample no. 5 of SSs. (D) Sample no. 2 of ASs. (E) Sample no. 4 of ASs. (F) Sample no. 7 of ASs.

Table 4. Micropore Fractal Dimensions Derived from the CA Experiment[a]

samples	lithologies	depth (m)	TOC (%)	K1	D1	R^2
no. 3	SS	929.82	2.99	0.5812	2.5812	0.9951
no. 8	SS	970.99	3.95	0.7044	2.7044	0.9973
no. 6	AS	966.26	5.98	0.433	2.4330	0.9930

[a]K1 represents the slope of a line; R^2 represents the degree of fit of the line; and D1 represents the micropore fractal dimension.

diagenesis, such as cementation and dissolution, the pore types are diverse and the pore structure of shales is more complex.

4.3.3. Fractal Dimensions of Macropores. The fractal dimensions of SS and AS are divided into three sections with pore sizes of 0.05−1 μm, 1−17 μm, and greater than 17 μm, which are D4, D5, and D6, respectively (Figure 10). The values of D4, D5, and D6 all range from 2 to 3, indicating the pore structure could be effectively characterized by the fractal dimensions of macropores. Fractal dimensions D4, D5, and D6 of SS range from 2.22 to 2.65, 2.07 to 2.09, and 2.36 to 2.56, respectively, with an average of 2.4, 2.08, and 2.43, respectively. The fractal dimensions of AS are D4 (2.25−2.41), D5 (2.06−

https://doi.org/10.1021/acs.energyfuels.1c01823
Energy Fuels 2021, 35, 15525−15544

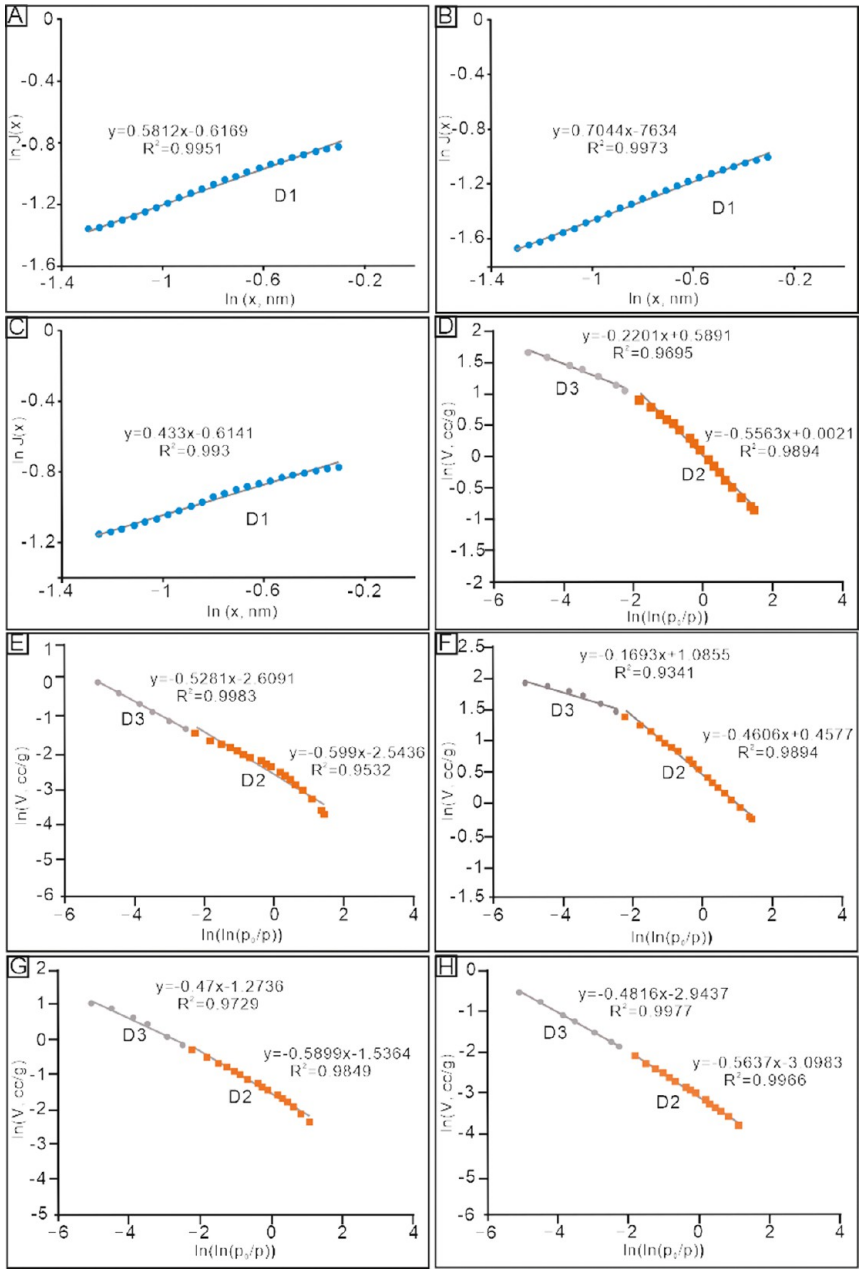

Figure 9. (A–C) Cross-plots of ln $J(x)$ and ln x calculated by the adsorption data of the CA experiment of the Yanchang Formation shales showing the fractal dimension D1. (A) Sample no. 3 of SSs. (B) Sample no. 8 of SSs. (C) Sample no. 6 of ASs. (D–I) Cross-plots were drawn by ln(ln(P_0/P)) and ln(V) calculated by the data from the adsorption branch of the NA experiment showing the fractal dimensions D2 and D3. (D) Sample no. 1 of SSs. (E) Sample no. 3 of SSs. (F) Sample no. 5 of SSs. (G) Sample no. 2 of ASs. (H) Sample no. 4 of ASs.

Table 5. Fractal Dimensions of Mesropores Calculated by the FHH Model of the NA Experiment[a]

			P/P_0 = 0.01–0.9			P/P_0 = 0.9–1		
samples	lithologies	depth (m)	K2	D2	R	K3	D3	R
no. 1	SS	877.36	−0.56	2.44	0.995	−0.22	2.78	0.985
no. 3	SS	929.82	−0.60	2.40	0.976	−0.53	2.47	0.999
no. 5	SS	939.46	−0.46	2.54	0.995	−0.17	2.83	0.967
			P/P_0 = 0.02–0.9			P/P_0 = 0.9–1		
samples	lithologies	depth (m)	K2	D2	R	K3	D3	R
no. 2	AS	927.97	−0.59	2.41	0.992	−0.47	2.53	0.986
no. 4	AS	935.02	−0.56	2.44	0.998	−0.48	2.52	0.999
no. 7	AS	970.29	−0.67	2.33	0.990	−0.24	2.76	0.984

[a]K2 and K3 represent the slope of a line; R^2 represents the degree of fit of the line; and D2–D3 represent the mesopore fractal dimensions.

https://doi.org/10.1021/acs.energyfuels.1c01823
Energy Fuels 2021, 35, 15525–15544

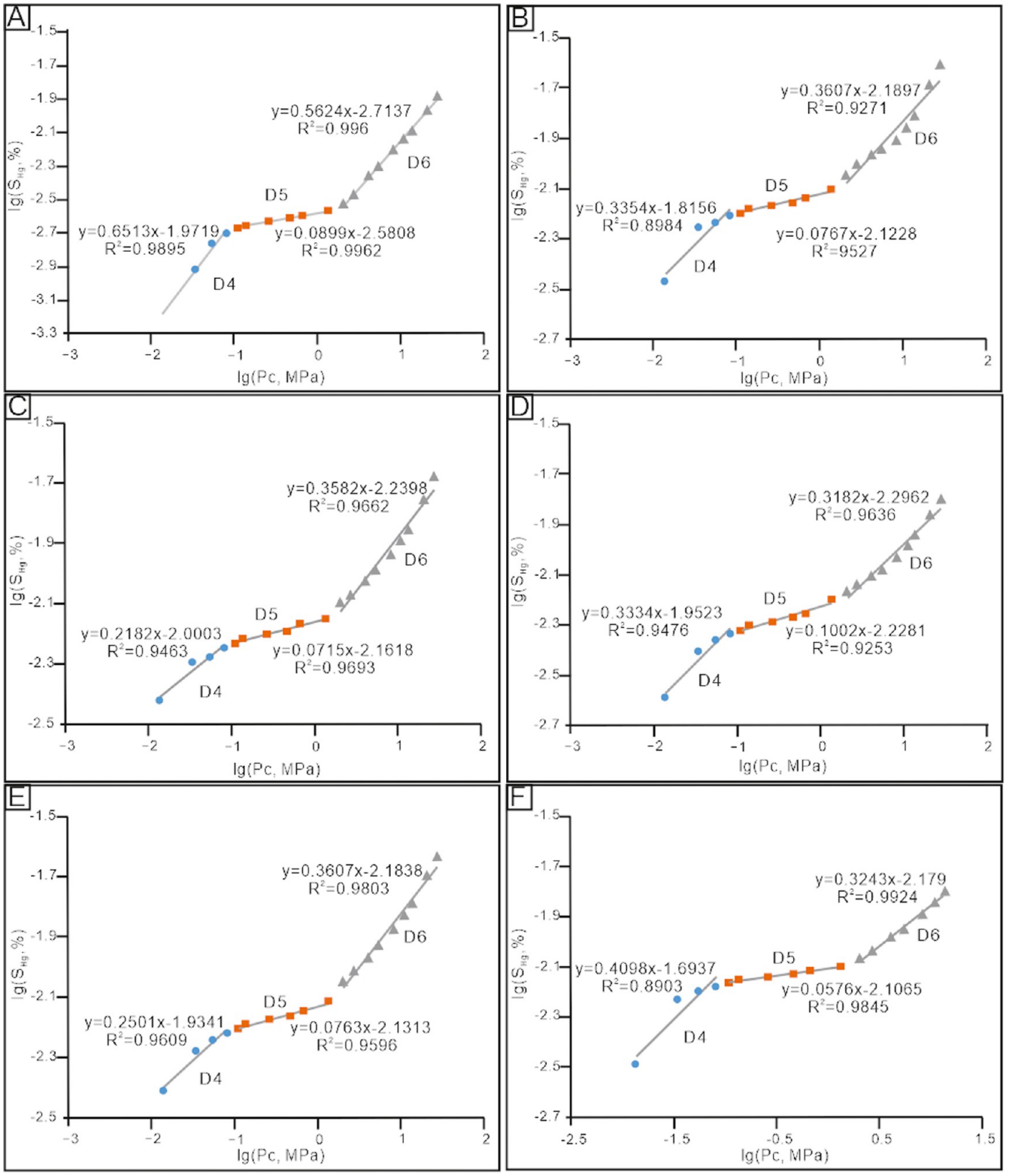

Figure 10. Plots of $\lg(P_c)$ vs $\ln(S_{Hg})$ reconstructed from the data of the HPMI experiment showing the fractal dimensions D4, D5, D6. (A) Sample no. 1 of SSs. (B) Sample no. 3 of SSs. (C) Sample no. 5 of SSs. (D) Sample no. 2 of ASs. (E) Sample no. 4 of ASs. (F) Sample no. 7 of ASs.

2.10), and D6 (2.32−2.36) and the average of D4, D5, and D6 is 2.4, 2.08, and 2.43, respectively (Table 6).

The fractal dimension of D4 is similar to D6, and D5 is smaller than D4 and D6, indicating that pore surfaces of smaller (0.05−1 μm) and larger (>17 μm) pores are rougher and pore structures are more complex, while those pores in the range of intermediate sizes (1−17 μm) have smoother pore surfaces and simpler pore structures.

The fractal dimensions D4 and D6 of SS are both larger than that of AS, indicating that the pore surface of SS is rougher with a more complex pore structure in a pore size of 0.05−1 μm and pore size > 17 μm. The fractal dimension D5 of SS is

https://doi.org/10.1021/acs.energyfuels.1c01823
Energy Fuels 2021, 35, 15525−15544

Table 6. Fractal Dimensions of the Macropore Derived from the Mercury Injection Branch of the HPMI Experiment[a]

		pore size 0.05−1 μm			pore size 1−17 μm			pore size >17 μm		
samples	lithology	K4	D4	R	K5	D5	R	K6	D6	R
no. 1	SS	0.6513	2.65	0.9947	0.0899	2.09	0.9981	0.5624	2.56	0.9980
no. 3	SS	0.3354	2.34	0.9478	0.0767	2.08	0.9761	0.3607	2.36	0.9629
no. 5	SS	0.2182	2.22	0.9728	0.0715	2.07	0.9845	0.3582	2.36	0.9830
no. 2	AS	0.3334	2.33	0.9734	0.1002	2.10	0.9619	0.3182	2.32	0.9816
no. 4	AS	0.2501	2.25	0.9803	0.0763	2.08	0.9796	0.3607	2.36	0.9901
no. 7	AS	0.4098	2.41	0.9436	0.0576	2.06	0.9922	0.3243	2.32	0.9962

[a]SS = siliceous shale; AS = argillaceous shale; K4, K5 and K6 represent the slope value of the fitting line; R^2 indicates the degree of fit of the line; and D4−D6 represent the macropore fractal dimensions.

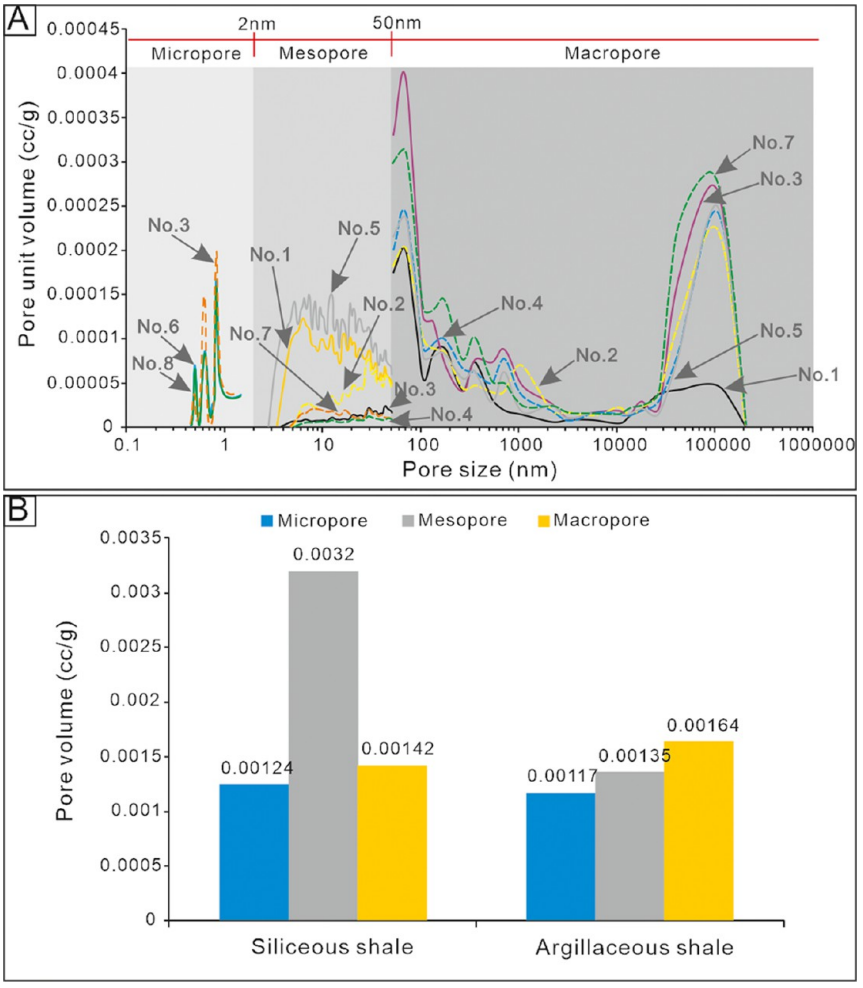

Figure 11. (A) Curve graph of the pore size and unit volume in the range of micropores, mesopores, and macropores of SSs and ASs. no. 1, no. 3, no. 5, and no. 8 are the samples of SSs, no. 2, no. 4, no. 6, and no. 7 are the samples of ASs. (B) Volumes of micropores, mesopores, and macropores of SSs and ASs.

similar to that of AS, indicating that the characteristics of the pore structure of SS are similar as that of AS in a pore size of 1−17 μm.

5. DISCUSSION

5.1. PSD Characteristics Combined CA, NA, and HPMI. Considering the different applicability of the three experiments to different pore ranges, using the pore diameters of 2 and 50 nm as the boundary, the experimental data of CA, NA, and HPMI were investigated to discuss the characteristic of the full range PSD.

The micropores of both SS and AS are concentrated in the range of 0.3−1.5 nm, and the peaks of the pore volume occur at pore sizes of 0.5, 0.6, and 0.8 nm, respectively. It shows that SS and AS have a small difference in micro-PSD. The pore volume of SS at 0.5 nm is higher than that of AS, while the pore volume at pore sizes of 0.6 and 0.8 nm is smaller than that of AS (Figure 11A). This is determined by the development of more OM in AS. The higher the content of OM, the higher the probability of developing large micropores. In addition, the intercrystalline micropores of clay minerals also contribute to the increase of the proportion of large micropores.

https://doi.org/10.1021/acs.energyfuels.1c01823
Energy Fuels 2021, 35, 15525−15544

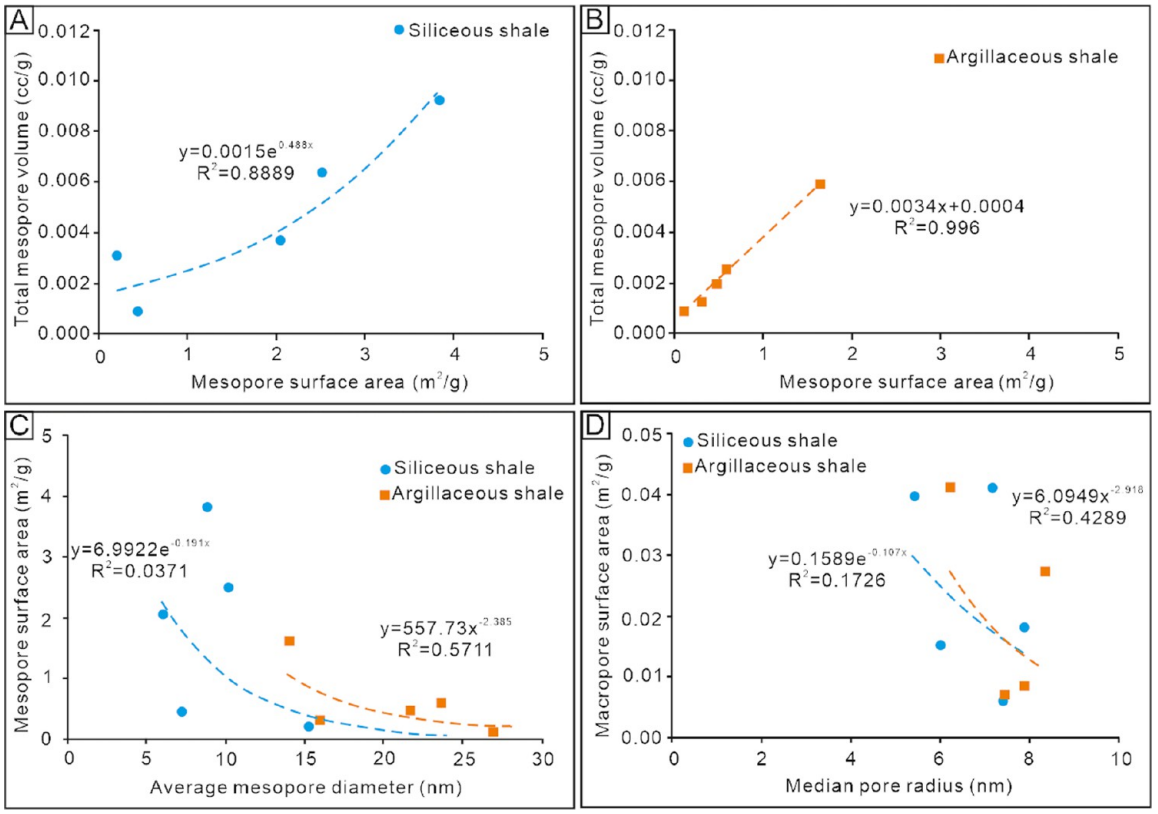

Figure 12. Relationships between mesopore surface area and (A) total volume of SS, (B) total volume of AS, and (C) average diameter of the mesopore obtained from NA. (D) Relationships between the median pore radius and macropore surface area obtained from NA.

The differences of the mesoporous distribution between SS and AS are the most obvious (Figure 11A). This may be related to the siliceous content. The content of quartz and feldspar in SS is higher and the grains are larger, and the intergranular and intragranular pores of quartz and feldspar are more developed, resulting in the significantly higher mesoporous volume of SS than that of AS. Except for sample no. 3, the mesoporous volume of SS increases at first, then decreases with the increase of the pore size, with the maximum value 0.0012 cc/g of pore size at 6−7 nm. The mesoporous volume of sample no. 3 of SS and AS is positively correlated with the pore size. The peak value appears within the scope of 27−30 nm, and the maximum value of the mesoporous volume is 0.00007−0.00008 cc/g. This may be because the content of siliceous minerals in sample no. 3 is higher than that of clay minerals, while the absolute clay mineral content is higher (Figure 3B). The mutual support between siliceous minerals and clay particles with larger particles is conducive to the formation of more mesoporous pores with larger pore sizes, thus increasing the volume of mesoporous pores.

The macropores of SS and AS are concentrated in the range of 50 nm−210 μm, with two peaks at pore sizes of 70 nm and 100 μm (Figure 11A). The maximum macropore volumes of SS are 0.00039 and 0.00027 cc/g, respectively, while those of AS are 0.00031 and 0.00028 cc/g, respectively.

In terms of the pore volume, the micropore (0.00124 cc/g), mesopore (0.0032 cc/g), and macropore (0.00142 cc/g) of SS contributes 21, 55, and 24%, respectively, to the total volume of pores, while the micropore, mesopore, and macropore volumes of AS are 0.00117, 0.00135, and 0.00164 cc/g, respectively, and the contribution rates are 28, 32, and 40%, respectively. Moreover, the micropore volume of the SS is slightly larger than that of AS, and the mesoporous volume of the SS is larger than that of AS, while the volume of the macropore is slightly smaller than that of AS (Figure 11B). The siliceous content of SS is high, and the intergranular and intragranular pores related to quartz and feldspar are mostly distributed in the mesoporous range. The high proportion of the siliceous content is beneficial to the increase of mesoporous volume. However, the TOC content of AS is higher than that of SS, and the dissolution of organic acids is conducive to the formation of larger macropores, thus increasing the proportion of macropore volume.

5.2. Relationships and Influence Factors for Pore Structure Parameters and Fractal Dimensions. There is an obvious positive correlation between the mesopore surface area and total mesopore volume obtained from NA, and the correlation coefficients (R^2) are 0.8889 of SS (Figure 12A) and 0.9996 of AS (Figure 12B). The average mesopore diameter increases with the decreasing of the mesopore surface area of AS, with an correlation coefficient R^2 of 0.5711 (Figure 12C). This indicates that with the increase of the average mesopore diameter, the total mesopore volume and mesopore surface area decrease. For macropores, the median pore radius shows a significant negative correlation with the macropore surface area of AS, with a correlation coefficient (R^2) of 0.4289 (Figure 12D). This indicates that with the increase of the median pore radius, the macropore surface area decreases, and the correlation coefficient is significant for AS.

The relationships between some parameters of the pore structure and fractal dimensions are shown in Figure 13. The average mesopore diameter shows a negative correlation with D2 (Figure 13A) and D3 (Figure 13B), especially for SS. It indicates that with the increase of the average mesopore

https://doi.org/10.1021/acs.energyfuels.1c01823
Energy Fuels 2021, 35, 15525−15544

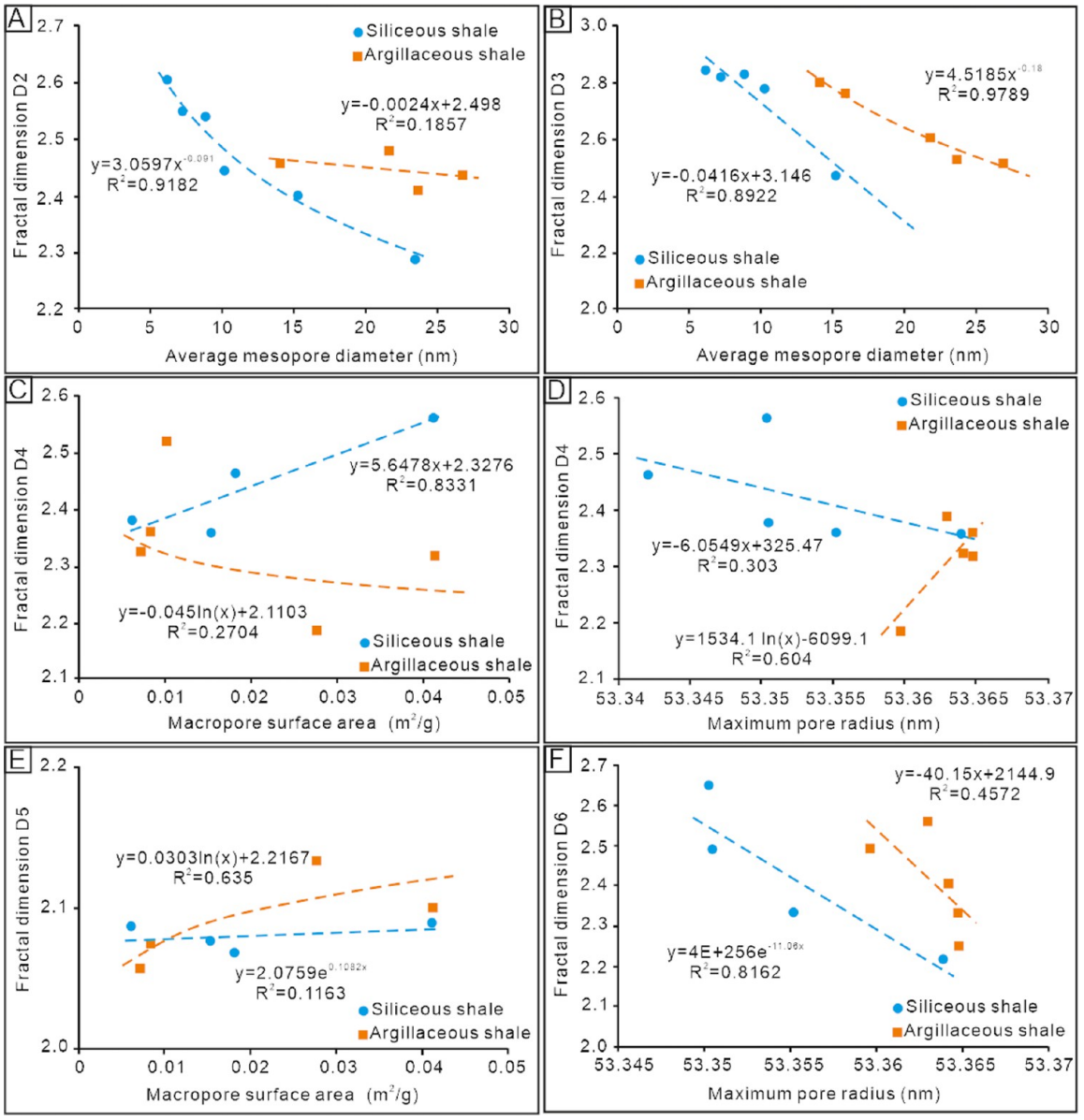

Figure 13. Relationships between fractal dimensions (D2−D6) and the most influential pore structure parameters, D2 and D3 and (A,B) average mesopore diameter derived from the NA experiment, D4 and (C) macropore surface area, (D) maximum pore radius, (E) D5 and macropore surface area, and (F) D6 and maximum pore radius.

diameter and the decrease of mesopore fractal dimensions, the complexity of the mesopore structure decreases. It shows an obvious positive correlation of the macropore surface area and D4 (Figure 13C) for SS, and a positive correlation of the maximum pore radius and D4 (Figure 13D) for AS. It reveals that a high macropore surface area and low maximum pore radius indicate a more complex pore structure of small macropores, both for SS and AS. D5 positively correlates with the macropore surface area (Figure 13E) of AS and there is a conspicuous correlation between D6 and maximum pore radius (Figure 13F) of SS.

As shown in Figure 14, except for the correlation of the quartz content and mesopore surface area of SS (Figure 14A), mesopore surface area (Figure 14A,E) of AS, and total mesopore volume (Figure 14B,F) of AS and SS both decrease as the quartz and clay content increases. With the increase in the feldspar content, the average mesopore diameter (Figure 14C) and maximum pore radius increase (Figure 14D), while the average mesopore diameter and maximum pore radius of AS decrease.

Figure 15 shows the correlations of mineral contents and fractal dimensions. The feldspar content shows negative correlations with fractal dimension D2 (Figure 15A) and fractal dimension D3 (Figure 15B) of SS, while feldspar content shows positive correlations with fractal dimension D2 and fractal dimension D3 (Figure 15A,B) of AS. There is also a positive relationship between D4 and quartz content of SS and AS (Figure 15C). For AS, clay minerals content shows an obvious positive correlation with D4 (Figure 15D), while the quartz content shows a negative correlation with D5 (Figure 15E), especially for SS. The feldspar content also shows an obvious positive relationship with D6 of AS and a negative correlation with D6 of SS (Figure 15F).

The above relationships indicate that quartz and clay minerals are bad for the mesopore volume development of AS, especially quartz minerals. The feldspar content shows a

https://doi.org/10.1021/acs.energyfuels.1c01823
Energy Fuels 2021, 35, 15525−15544

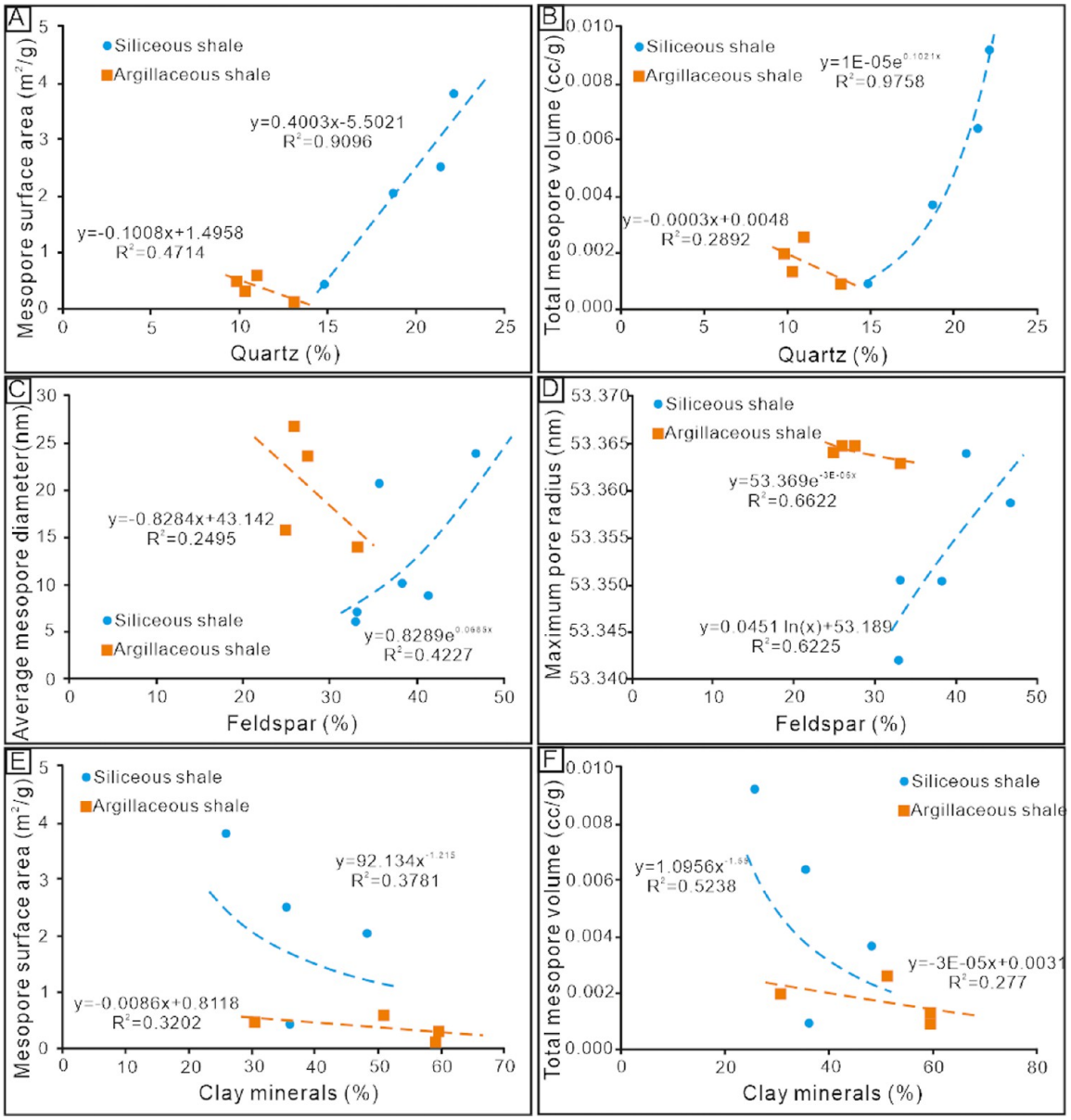

Figure 14. Relationships between pore structure parameter and mineral content. Correlations of the content of quartz mineral and (A) mesopore surface area, (B) total volume of mesopore. Correlations of feldspar content and (C) average mesopore diameter, and (D) maximum pore radius. Correlations of mineral content of clay and (E) mesopore surface area and (F) total volume of the mesopore.

negative relationship with a mesopore size of AS. Clay minerals also have a significant adverse effect on the pore development of SS, while quartz and feldspar contents are conducive to the development of the mesopore. The development of feldspar reduces the complexity of the mesopore structure of SS, while a higher feldspar content leads to a more complex mesoporous structure of AS. Moreover, the development of quartz and clay minerals lead to a more complex structure of the small macropore, especially for AS, while the development of quartz minerals reduces the complexity of median macropores to some extent. The pore structure complexity of large macropores increases with the increase of the feldspar content for AS, while it shows an inverse relationship for SS.

The development of quartz and clay minerals can block intergranular pores, resulting in a reduction in the pore volume of AS dominated by cementation. Due to weak dissolution, the development of feldspar is not conducive to the increase of the pore size for AS. For SS, larger quartz grains act as supports and hinder the development of clay minerals, reducing the damage to the primary pores. The high content of feldspar in SS increases the probability of dissolution, which makes pore size expand.

Smaller feldspar grains in AS increase the types of small pores associated with feldspar, while larger feldspar grains are prone to form microfractures, making the pore structure more complex. For SS, the complexity of the mesoporous pore structure was reduced by reducing the proportion of mesoporous pores with a larger size and higher content of feldspar particles. Dissolution can enlarge the pore size of microfractures to close to larger macropores, thus reducing the complexity of the pore structure of larger macropores. Feldspar mineral is prone to dissolution which helps to forms secondary pores and increase pore volume (Figure 4B,H). The dissolution of feldspar can expand small pores into large

https://doi.org/10.1021/acs.energyfuels.1c01823
Energy Fuels 2021, 35, 15525−15544

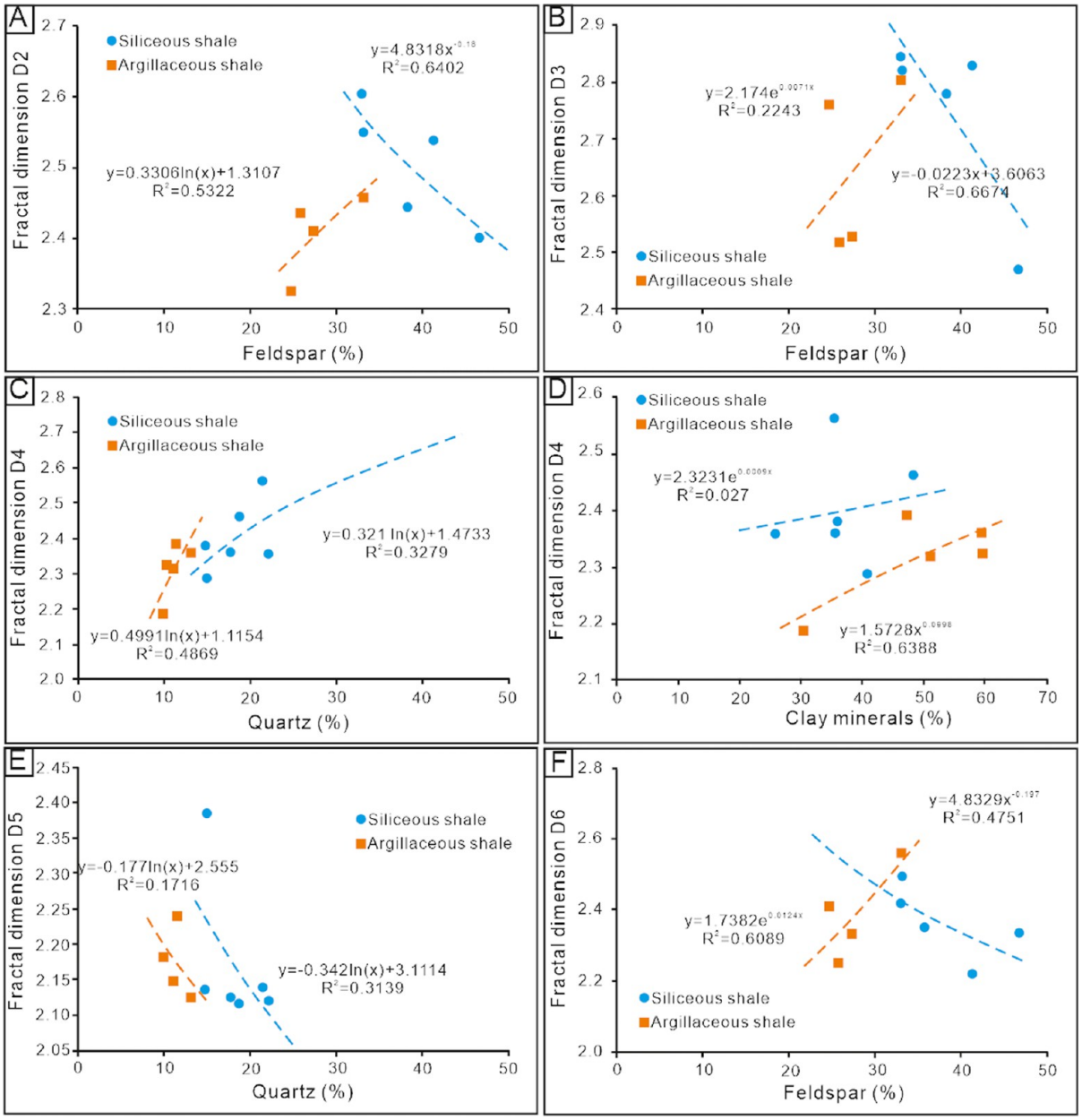

Figure 15. Relationships of the mineral content and fractal dimensions. Correlations of mineral content of feldspar and fractal dimension (A) D2 and (B) D3. Correlations of D4 and (C) quartz content and (D) clay minerals. (E) Correlations of quartz content and fractal dimension D5. (F) Correlations of feldspar content and fractal dimension D6.

pores; connect independent pores (Figure 4H); and reduce the complexity of the pore structure for SS. Quartz and clay minerals are more likely to show interpenetrating contact relations with each other (Figure 4G). Moreover, even quartz will squeeze and deform the clay minerals, resulting in irregular changes in the remaining pore size and connectivity, making the small macropore structure complex. For medium-sized macropores, quartz is more likely to provide support and protection to reduce the complexity of the pore structure.

5.3. Influence of Mineral Composition and Pore Structure on Petrophysical Properties. The relationships between the pore structure parameters and petrophysical properties (i.e., porosity and permeability) are illustrated by cross-plots shown in Figure 16. As Figure 16 shows, a negative relationship is found between the average mesopore diameter obtained from NA and porosity, with a correlation coefficient (R^2) of 0.9222 (Figure 16A) of AS, while a positive relationship of the average mesopore diameter and porosity of SS was found (Figure 16A). Permeability shows negative correlations with the macropore surface area (Figure 16B) of SS and AS. Among the relationships between the petrophysical property and fractal dimensions, the fractal dimension D4 is negatively correlated with the porosity of SS, with a correlation coefficient (R^2) of 0.6643, while the relationship is weak for AS (Figure 16C). Fractal dimension D3 is negatively related with the permeability of SS (R^2 = 0.9881), but D3 shows a positive correlation with AS (R^2 = 0.4343) (Figure 16D). These indicate that the increase of the average mesopore diameter and the decrease of the macropore surface area make porosity and permeability of SS increase, while the decrease of the average mesopore diameter and macropore surface area makes porosity and permeability of AS increase. Moreover, the

https://doi.org/10.1021/acs.energyfuels.1c01823
Energy Fuels 2021, 35, 15525−15544

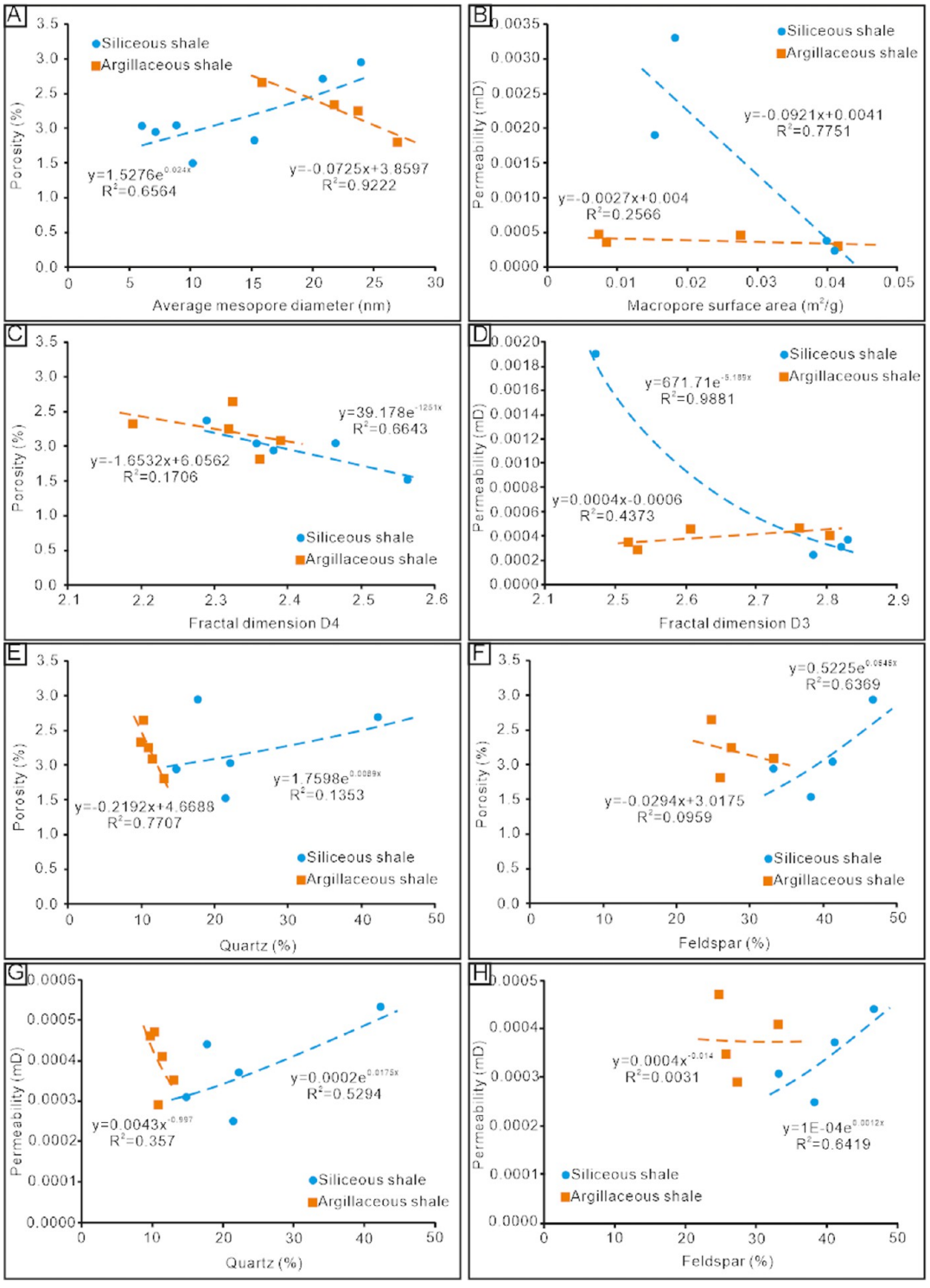

Figure 16. Relationships between the petrophysical property and fractal dimensions and mineral contents. Correlations of porosity and (A) average mesopore diameter, (C) fractal dimension D4, (E) quartz content, (F) feldspar content. Correlations of permeability and (B) macropore surface area, (D) fractal dimension D3, (G) quartz content, and (H) feldspar content.

decrease of the pore structure complexity of small macropores will increase the porosity. More complex mesoporous pore structures will reduce permeability, while the relationship is reversed for AS. This is because the larger the fractal dimension, the more complex is the pore type or the wider the PSD. When the proportion of the small pore size is high, the overall pore volume will decrease, and thus the porosity will decrease, especially the SS with more mesopores.

Figure 16 shows the relationships between mineral composition and petrophysical properties. Porosity shows an obvious negative relationship with quartz content (Figure 16E), weak negative correlation with feldspar content (Figure 16F) of AS, while feldspar content shows significant positive correlations with porosity (Figure 16F) for SS. There is a negative correlation between permeability and quartz content of AS (Figure 16G), while higher quartz and feldspar content

https://doi.org/10.1021/acs.energyfuels.1c01823
Energy Fuels 2021, 35, 15525−15544

increases permeability for SS (Figure 16G,H). It indicates that the development of quartz is not conducive to improve petrophysical properties of AS. This may be because quartz is not easily affected by dissolution and development of quartz might occupy the rest of the reservoir space. The development of feldspar is conducive to improve petrophysical properties. Feldspar minerals were dissolved by organic acids and secondary pores were generated (Figure 4H), which can increase pore volume and form a throat between pores or expand throat, and thus porosity and permeability both are improved.

6. CONCLUSIONS

(1) The lacustrine shale "Zhangjiatan Shale" can be divided into the SS and the AS by the relative content of siliceous and argillaceous minerals. Inorganic pores (i.e., interparticle and intraparticle pores, intercrystalline pores, and interlamellar pores), OM pores, and microfractures are developed in both SS and AS.

(2) The surface areas of mesopores and macropores and average macropore radius in AS are slightly smaller than that in SS, while the average mesopore size, micropore surface area, and volume of AS are larger than those of SS. The largest pore unit volume appears at 70 nm or 100 μm of both SS and AS.

(3) The micropore, mesopore, and macropore of SS contribute to 21, 55, and 24% of total pore volume, while the contribution rates of AS are 28, 32, and 40%, respectively. The mesoporous volume of SS is obviously larger than that of AS, while the volume of macropore is slightly smaller than that of AS.

(4) The fractal dimension D2 to D6 can effectively characterize the pore structure. Larger pores have rougher pore surfaces and more complex pore structures in the range of mesopores. For macropores, pore surfaces of smaller (0.05−1 μm) and larger (>17 μm) pores are rougher and pore structures are more complex. The pore surface of SS is rougher, and the pore structure is more complex.

(5) Average mesopore diameter, macropore surface area, and fractal dimensions D3 and D4 show a significant influence on petrophysical properties. The development of quartz makes the pore structure more complex and reduces the porosity and permeability, especially for AS, while the development of feldspar reduces the complexity of the pore structure and improves the petrophysical properties, especially for SS.

AUTHOR INFORMATION

Corresponding Author

Qing Li − *State Key Laboratory of Petroleum Resources and Prospecting, China University of Petroleum (Beijing), Beijing 102249, China; College of Geosciences, China University of Petroleum, Beijing 102249, China;* orcid.org/0000-0002-7223-4370; Email: liqing@cup.edu.cn, luhaocup@163.com

Authors

Hao Lu − *State Key Laboratory of Petroleum Resources and Prospecting, China University of Petroleum (Beijing), Beijing 102249, China; College of Geosciences, China University of Petroleum, Beijing 102249, China*

Dongdong Xia − *Petroleum Exploration and Development Institute of SINOPEC, Beijing 100083, China*

Dali Yue − *State Key Laboratory of Petroleum Resources and Prospecting, China University of Petroleum (Beijing), Beijing 102249, China; College of Geosciences, China University of Petroleum, Beijing 102249, China;* orcid.org/0000-0001-8918-9513

Shenghe Wu − *State Key Laboratory of Petroleum Resources and Prospecting, China University of Petroleum (Beijing), Beijing 102249, China; College of Geosciences, China University of Petroleum, Beijing 102249, China*

Wurong Wang − *State Key Laboratory of Petroleum Resources and Prospecting, China University of Petroleum (Beijing), Beijing 102249, China; College of Geosciences, China University of Petroleum, Beijing 102249, China*

Xuemei Zhang − *State Key Laboratory of Petroleum Resources and Prospecting, China University of Petroleum (Beijing), Beijing 102249, China; College of Geosciences, China University of Petroleum, Beijing 102249, China*

Complete contact information is available at: https://pubs.acs.org/10.1021/acs.energyfuels.1c01823

Notes

The authors declare no competing financial interest.

ACKNOWLEDGMENTS

This study was financially supported by the National Science and Technology Special (grant no. 2017ZX05049-006-001), the National Natural Science Foundation of China (grant no. 41602137), the Strategic Cooperation Technology Projects of CNPC and CUPB (ZLZX2020-02), and Science Foundation of China University of Petroleum, Beijing (no. 2462020YXZZ022). The authors also greatly appreciate Petroleum Exploration and Development Institute of SINOPEC for providing samples and data access and for permission to publish the results.

REFERENCES

(1) Chen, S.; Zhu, Y.; Wang, H.; Liu, H.; Wei, W.; Fang, J. Shale gas reservoir characterization: a typical case in the southern Sichuan Basin of China. *Energy* **2011**, *36*, 6609−6616.

(2) Zhang, J.; Li, X.; Zhang, G.; Zou, X.; Wang, F.; Tang, Y. Microstructural investigation of different nanopore types in marine-continental transitional shales: Examples from the Longtan formation in Southern Sichuan Basin, south China. *Mar. Pet. Geol.* **2019**, *110*, 912−927.

(3) Clarkson, C. R.; Jensen, J. L.; Chipperfield, S. Unconventional gas reservoir evaluation: what do we have to consider? *J. Nat. Gas Sci. Eng.* **2012**, *8*, 9−33.

(4) Liu, X.; Xiong, J.; Liang, L. Investigation of pore structure and fractal characteristics of organic-rich Yanchang formation shale in central China by nitrogen adsorption/desorption analysis. *J. Nat. Gas Sci. Eng.* **2015**, *22*, 62−72.

(5) Clarkson, C. R.; Solano, N.; Bustin, R. M.; Bustin, A. M. M.; Chalmers, G. R. L.; He, L.; Melnichenko, Y. B.; Radliński, A. P.; Blach, T. P. Pore structure characterization of North American shale gas reservoirs using USANS/SANS, gas adsorption, and mercury intrusion. *Fuel* **2013**, *103*, 606−616.

(6) Lai, J.; Wang, G.; Wang, Z.; Chen, J.; Pang, X.; Wang, S.; Zhou, Z.; He, Z.; Qin, Z.; Fan, X. A review on pore structure characterization in tight sandstones. *Earth-Sci. Rev.* **2018**, *177*, 436−457.

(7) Rouquerol, J.; Avnir, D.; Fairbridge, C. W.; Everett, D. H.; Haynes, J. M.; Pernicone, N.; Ramsay, J. D. F.; Sing, K. S. W.; Unger,

K. K. Recommendations for the characterization of porous solids (Technical Report). *Pure Appl. Chem.* **1994**, *66*, 1739−1758.
(8) Bernard, S.; Horsfield, B.; Schulz, H.-M.; Wirth, R.; Schreiber, A.; Sherwood, N. Geochemical evolution of organic-rich shales with increasing maturity: A STXM and TEM study of the Posidonia Shale (Lower Toarcian, northern Germany). *Mar. Pet. Geol.* **2012**, *31*, 70−89.
(9) Wei, X.; Liu, R.; Zhang, T.; Liang, X. Micropores structure characteristics and development control factors of shale gas reservoir: a case of Longmaxi Formation in XX area of southern Sichuan and northern Guizhou. *J. Nat. Gas Geosci.* **2013**, *24*, 1048−1059.
(10) Wu, J.; Yu, B.; Zhang, J.; Li, Y. Pore characteristics and controlling factors in the organic-rich shale of the Lower Silurian Longmaxi Formation revealed by samples from a well in southeastern Chongqing. *J. Earth Sci. Front.* **2013**, *20*, 260−269.
(11) Wang, W.; Yue, D.; Eriksson, K. A.; Qu, X.; Li, W.; Lv, M.; Zhang, J.; Zhang, X. Quantification and Prediction of Pore Structures in Tight Oil Reservoirs Based on Multifractal Dimensions from Integrated Pressure- and Rate-Controlled Porosimetry for the Upper Triassic Yanchang Formation, Ordos Basin, China. *Energy Fuels* **2020**, *34*, 4366−4383.
(12) Hazra, B.; Vishal, V.; Singh, D. P. Applicability of Low-Pressure CO_2 and N_2 Adsorption in Determining Pore Attributes of Organic-Rich Shales and Coals. *Energy Fuels* **2021**, *35*, 456−464.
(13) Jia, B.; Tsau, J.-S.; Barati, R. Different Flow Behaviors of Low-Pressure and High-Pressure Carbon Dioxide in Shales. *SPE J.* **2018**, *23*, 1452−1468.
(14) Chalmers, G. R. L.; Bustin, R. M. The organic matter distribution and methane capacity of the Lower Cretaceous strata of Northeastern British Columbia, Canada. *Int. J. Coal Geol.* **2007**, *70*, 223−239.
(15) Chalmers, G. R.; Bustin, R. M.; Power, I. M. Characterization of gas shale pore systems by porosimetry, pycnometry, surface area, and field emission scanning electron microscopy/transmission electron microscopy image analyses: examples from the Barnett, Woodford, Haynesville, Marcellus, and Doig units. *AAPG Bull.* **2012**, *96*, 1099−1119.
(16) Chalmers, G. R. L.; Ross, D. J. K.; Bustin, R. M. Geological controls on matrix permeability of Devonian Gas Shales in the Horn River and Liard basins, northeastern British Columbia, Canada. *Int. J. Coal Geol.* **2012**, *103*, 120−131.
(17) Ross, D. J. K.; Bustin, R. M. Shale gas potential of the Lower Jurassic Gordondale Member, northeastern British Columbia, Canada. *Bull. Can. Pet. Geol.* **2007**, *55*, 51−75.
(18) Ross, D. J. K.; Bustin, R. M. The importance of shale composition and pore structure upon gas storage potential of shale gas reservoirs. *Mar. Pet. Geol.* **2009**, *26*, 916−927.
(19) Peng, S.; Hu, Q.; Dultz, S.; Zhang, M. Using X-ray computed tomography in pore structure characterization for a Berea sandstone: resolution effect. *J. Hydrol.* **2012**, *472*−*473*, 254−261.
(20) Wang, X.; Hou, J.; Song, S.; Wang, D.; Gong, L.; Ma, K.; Liu, Y.; Li, Y.; Yan, L. Combining pressure-controlled porosimetry and rate-controlled porosimetry to investigate the fractal characteristics of full-range pores in tight oil reservoirs. *J. Pet. Sci. Eng.* **2018**, *171*, 353−361.
(21) Mandelbrot, B. B.; Passoja, D. E.; Paullay, A. J. Fractal character of fracture surfaces in porous media. *Nature* **1984**, *308*, 721−722.
(22) Lai, J.; Wang, G. Fractal analysis of tight gas sandstones using high-pressure mercury intrusion techniques. *J. Nat. Gas Sci. Eng.* **2015**, *24*, 185−196.
(23) Li, A.; Ding, W.; He, J.; Dai, P.; Yin, S.; Xie, F. Investigation of pore structure and fractal characteristics of organic-rich shale reservoirs: A case study of Lower Cambrian Qiongzhusi formation in Malong block of eastern Yunnan Province, South China. *Mar. Pet. Geol.* **2016**, *70*, 46−57.
(24) Chandra, D.; Vishal, V. A comparison of nano-scale pore attributes of Barakar Formation gas shales from Raniganj and Wardha Basin, India using low pressure sorption and FEG-SEM analysis. *J. Nat. Gas Sci. Eng.* **2020**, *81*, 103453.
(25) Ji, W.; Song, Y.; Jiang, Z.; Meng, M.; Liu, Q.; Chen, L.; Wang, P.; Gao, F.; Huang, H. Fractal characteristics of nano-pores in the lower Silurian Longmaxi shales from the upper Yangtze Platform, south China. *Mar. Pet. Geol.* **2016**, *78*, 88−98.
(26) Xian, B.; Wang, J.; Gong, C.; Yin, Y.; Chao, C.; Liu, J.; Zhang, G.; Yan, Q. Classification and sedimentary characteristics of lacustrine hyperpycnal channels: Triassic outcrops in the south Ordos Basin, central China. *Sediment. Geol.* **2018**, *368*, 68−82.
(27) Zhang, T.; Hu, S.; Bu, Q.; Bai, B.; Tao, S.; Chen, Y.; Pan, Z.; Lin, S.; Pang, Z.; Xu, W.; et al. Effects of lacustrine depositional sequences on organic matter enrichment in the Chang 7 Shale, Ordos Basin, China. *Mar. Pet. Geol.* **2021**, *124*, 104778.
(28) Gu, Y.; Li, X.; Yang, S.; Wan, Q. Microstructure Evolution of Organic Matter and Clay Minerals in Shales with Increasing Thermal Maturity. *Acta Geol. Sin.* **2020**, *94*, 280−289.
(29) Liu, F.; Zhu, X.; Li, Y.; Xue, M.; Sun, J. Sedimentary facies analysis and depositional model of gravity-flow deposits of the Yanchang Formation, southwestern Ordos Basin, NW China. *Aust. J. Earth Sci.* **2016**, *63*, 885−902.
(30) Lu, H.; Li, Q.; Yue, D.; Wu, S.; Fu, Y.; Tang, R.; Zhang, Z. Study on optimal selection of porosity logging interpretation methods for Chang 73 segment of the Yanchang Formation in the southwestern Ordos Basin, China. *J. Pet. Sci. Eng.* **2021**, *198*, 108153.
(31) Yang, Y.; Li, W.; Ma, L. Tectonic and stratigraphic controls of hydrocarbon systems in the Ordos basin: a multicycle cratonic basin in central China. *AAPG Bull.* **2005**, *89*, 255−269.
(32) He, C.; Ji, L.; Wu, Y.; Su, A.; Zhang, M. Characteristics of hydrothermal sedimentation process in the yanchang formation, south ordos basin, China: evidence from element geochemistry. *Sediment. Geol.* **2016**, *345*, 33−41.
(33) Wang, C.; Wang, Q.; Chen, G.; He, L.; Xu, Y.; Chen, L.; Chen, D. Petrographic and geochemical characteristics of the lacustrine black shales from the upper Triassic Yanchang formation of the Ordos basin, China: implications for the organic matter accumulation. *Mar. Pet. Geol.* **2017**, *86*, 52−65.
(34) Wu, H.; Zhang, C.; Ji, Y.; Liu, R.; Wu, H.; Zhang, Y.; Geng, Z.; Zhang, Y.; Yang, J. An improved method of characterizing the pore structure in tight oil reservoirs: Integrated NMR and constant-rate controlled porosimetry data. *J. Pet. Sci. Eng.* **2018**, *166*, 778−796.
(35) Dou, W.; Liu, L.; Wu, K.; Xu, Z.; Liu, X.; Feng, X. Diagenetic heterogeneity, pore throats characteristic and their effects on reservoir quality of the Upper Triassic tight sandstones of Yanchang Formation in Ordos Basin, China. *Mar. Pet. Geol.* **2018**, *98*, 243−257.
(36) Li, Q.; Wu, S.; Xia, D.; You, X.; Zhang, H.; Lu, H. Major and trace element geochemistry of the lacustrine organic-rich shales from the Upper Triassic Chang 7 Member in the southwestern Ordos Basin, China: Implications for paleoenvironment and organic matter accumulation. *Mar. Pet. Geol.* **2020**, *111*, 852−867.
(37) Mastalerz, M.; Hampton, L.; Drobniak, A.; Loope, H. Significance of analytical particle size in low-pressure N_2 and CO_2 adsorption of coal and shale. *Int. J. Coal Geol.* **2017**, *178*, 122−131.
(38) Li, D.; Li, R.; Zhu, Z.; Wu, X.; Cheng, J.; Liu, F.; Zhao, B. Origin of organic matter and paleo-sedimentary environment reconstruction of the Triassic oil shale in Tongchuan City, southern Ordos Basin (China). *Fuel* **2017**, *208*, 223−235.
(39) Torabi, A.; Fossen, H.; Braathen, A. Insight into petrophysical properties of deformed sandstone reservoirs. *AAPG Bull.* **2013**, *97*, 619−637.
(40) Guo, X.; Huang, Z.; Zhao, L.; Han, W.; Ding, C.; Sun, X.; Yan, R.; Zhang, T.; Yang, X.; Wang, R. Pore structure and multi-fractal analysis of tight sandstone using MIP, NMR and NMRC methods: A case study from the Kuqa depression, China. *J. Pet. Sci. Eng.* **2019**, *178*, 544−558.
(41) Schlueter, E. M.; Zimmerman, R. W.; Witherspoon, P. A.; Cook, N. G. W. The fractal dimension of pores in sedimentary rocks and its influence on permeability. *Eng. Geol.* **1997**, *48*, 199−215.
(42) Wang, M.; Xue, H.; Tian, S.; Wilkins, R. W. T.; Wang, Z. Fractal characteristics of Upper Cretaceous lacustrine shale from the Songliao Basin, NE China. *Mar. Pet. Geol.* **2015**, *67*, 144−153.

https://doi.org/10.1021/acs.energyfuels.1c01823
Energy Fuels 2021, 35, 15525−15544

(43) Li, K. Analytical derivation of Brooks-Corey type capillary pressure models using fractal geometry and evaluation of rock heterogeneity. *J. Pet. Sci. Eng.* **2010**, *73*, 20−26.
(44) Jaroniec, M.; Gilpin, R. K.; Choma, J. Correlation between microporosity and fractal dimension of active carbons. *Carbon* **1993**, *31*, 325−331.
(45) Dubinin, M. M.; Stoeckli, H. F. Homogeneous and heterogeneous micropore structures in carbonaceous adsorbents. *J. Colloid Interface Sci.* **1980**, *75*, 34−42.
(46) Stoeckli, H. F.; Ballerini, L.; De Bernardini, S. On the evolution of micropore widths and areas in the course of activation. *Carbon* **1989**, *27*, 501−502.
(47) Hu, J.; Tang, S.; Zhang, S. Investigation of pore structure and fractal characteristics of the Lower Silurian Longmaxi shales in western Hunan and Hubei Provinces in China. *J. Nat. Gas Sci. Eng.* **2016**, *28*, 522−535.
(48) Yang, F.; Ning, Z.; Liu, H. Fractal characteristics of shales from a shale gas reservoir in the Sichuan Basin, China. *Fuel* **2014**, *115*, 378−384.
(49) Pfeifer, P.; Wu, Y.; Cole, M. W.; Krim, J. Multilayer adsorption on a fractally rough surface. *Phys. Rev. Lett.* **1989**, *62*, 1997.
(50) Qi, H.; Ma, J.; Wong, P.-z. Adsorption isotherms of fractal surfaces. *Colloids Surf., A* **2002**, *206*, 401−407.
(51) Song, Z.; Liu, G.; Yang, W.; Zou, H.; Sun, M.; Wang, X. Multi-fractal distribution analysis for pore structure characterization of tight sandstone-A case study of the Upper Paleozoic tight formations in the Longdong District, Ordos Basin. *Mar. Pet. Geol.* **2018**, *92*, 842−854.
(52) Sing, K. S. W.; Everett, D. H.; Haul, R. A. W.; Moscou, L.; Pierotti, R. A.; Rouquérol, J.; Siemieniewska, T. Reporting physisorption data for gas/solid systems with special reference to the determination of surface area and porosity (recommendations 1984). *Pure Appl. Chem.* **1985**, *57*, 603−619.

https://doi.org/10.1021/acs.energyfuels.1c01823
Energy Fuels 2021, 35, 15525−15544